I R A M P
4(2), December 2013, pp. 121-177

ISSN: 2229-3159

Applications of the Classical Two-Coulomb-Center Systems to Atomic/Molecular Physics

N. KRYUKOV[1] AND E. OKS[1]

[1]*Physics Department, 206 Allison Lab, Auburn University, Auburn, AL 36849, USA*

ABSTRACT: We review recent advances in the classical studies of the two-Coulomb-center (TCC) systems consisting of two nuclei of charges Z and Z' and an electron in a circular or a helical state centered on the internuclear axis. These systems represent diatomic Rydberg quasimolecules encountered, e.g., in plasmas containing more than one kind of multicharged ions. Diatomic Rydberg quasimolecules are one of the most fundamental theoretical playgrounds for studying charge exchange. Charge exchange and crossings of corresponding energy levels that enhance charge exchange are strongly connected with problems of energy losses and of diagnostics in high temperature plasmas; besides, charge exchange is one of the most effective mechanisms for population inversion in the soft *x*-ray and *VUV* ranges. The classical approach is well-suited for Rydberg quasimolecules. First, we considered diatomic Rydberg quasimolecules subjected to a static electric field parallel to the internuclear axis. We found the appearance of an additional (fourth) term, which was absent at the zero field, and which had a *V*-type crossing with the lowest term. We also found *X*-type crossings (absent at the zero field) which significantly enhance charge exchange. Second, we studied effects of the electron screening in plasmas on diatomic Rydberg quasimolecules. We found that the screening stabilizes the nuclear motion for $Z = 1$ and destabilizes it for $Z > 1$. We also found that a so-called continuum lowering in plasmas was impeded by the screening, creating the effect similar to that of the magnetic field and opposite to that of the electric field. The continuum lowering plays a key role in calculations of the equation of state, partition function, bound-free opacities, and other collisional atomic transitions in plasmas. Third, we considered diatomic Rydberg quasimolecules in a laser field. For the situation where the laser field is linearly-polarized along the internuclear axis, we found an analytical solution for the stable helical motion of the electron valid for wide ranges of the laser field strength and frequency. We also found resonances, corresponding to a laser-induced unstable motion of the electron, that result in the destruction of the helical states. For the case of a circularly-polarized field, polarization plane being perpendicular to the internuclear axis, we found an analytical solution for circular Rydberg states valid for wide ranges of the laser field strength and frequency. For this case we demonstrated also that there is a red shift of the primary spectral component. We showed that both under the linearly-polarized laser field and under the circularly-polarized laser field, in the electron radiation spectrum in the addition to the primary spectral component at (or near) the unperturbed revolution frequency of the electron, there appear satellites. Under a laser field of a known strength, in the case of the linear polarization the observation of the satellites would be the confirmation of the helical electronic motion in the Rydberg quasimolecule, while in the case of the circular polarization the observation of the red shift of the primary spectral component would be the confirmation of the specific type of the phase modulation of the electronic motion. Conversely, if the laser field strength is unknown, both the relative intensities of the satellites and the red shift of the primary spectral component could be used for measuring the laser field strength. Fourth, we considered TCC systems consisting of a proton, muon and an electron. We found that a muonic hydrogen atom can attach an electron, with the muon and electron being in circular states. The technique of the separation of rapid and slow subsystems was used, where the muon represented the *rapid* subsystem and the electron the *slow* subsystem. We showed that the spectral lines emitted by the muon experience a red shift compared to the corresponding spectral lines in a muonic hydrogen atom. Observing this red shift should be one of the ways to detect the formation of such muonic-electronic negative hydrogen ions. Studies of muonic atoms and molecules, where one of the electrons is substituted by the heavier lepton μ^-, have several applications, such as muon-catalyzed fusion, a laser-control of nuclear processes, and a search for strongly interacting massive particles proposed as dark matter candidates and as candidates for the lightest supersymmetric particle.

1. INTRODUCTION: TWO-COULOMB CENTER SYSTEMS REPRESENTING DIATOMIC RYDBERG QUASIMOLECULES

Charge exchange and crossings of corresponding energy levels that enhance charge exchange are strongly connected with problems of energy losses and of diagnostics in high temperature plasmas – see, e.g., [1.1, 1.2] and references therein. Besides, charge exchange was proposed as one of the most effective mechanisms for population inversion in the soft *x*-ray and *VUV* ranges [1.3-1.6]. One of the most fundamental theoretical playgrounds for studying charge exchange is the problem of electron terms in the field of two stationary Coulomb centers (TCC) of charges Z and Z' separated by a distance R. It presents fascinating atomic physics: the terms can have crossings and quasicrossings.

The crossings are due to the fact that that the well-known Neumann-Wigner general theorem on the impossibility of crossing of terms of the same symmetry [1.7] is not valid for the TCC problem of $Z' \neq Z$ – as shown in paper [1.8]. Physically it is here a consequence of the fact that the TCC problem allows a separation of variables in the elliptic coordinates [1.8]. As for the quasicrossings, they occur when two wells, corresponding to separated Z- and Z'-centers, have states Ψ and Ψ', characterized by the same energies $E = E'$, by the same magnetic quantum numbers $m = m'$, and by the same radial elliptical quantum numbers $k = k'$ [1.9-1.11]. In this situation, the electron has a much larger probability of tunneling from one well to the other (i.e., of charge exchange) as compared to the absence of such degeneracy.

These rich features of the TCC problem also manifest in a different area of physics such as plasma spectroscopy as follows. A quasicrossing of the TCC terms, by enhancing charge exchange, can result in unusual structures (dips) in the spectral line profile emitted by a Z-ion from a plasma consisting of both Z- and Z'-ions, as was shown theoretically and experimentally [1.12-1.17]. From the experimental width of these dips it is possible to determine rate coefficients of charge exchange between multicharged ions, which is a fundamental reference data virtually inaccessible by other experimental methods [1.17].

Before year 2000, the paradigm was that the above sophisticated features of the TCC problem and its flourishing applications were inherently quantum phenomena. But then in year 2000, papers [1.18, 1.19] were published presenting a purely classical description of both the crossings of energy levels in the TCC problem and the dips in the corresponding spectral line profiles caused by the crossing (via enhanced charge exchange). These classical results were obtained analytically based on first principles without using any model assumptions.

In the classical studies the TCC systems represent diatomic Rydberg quasimolecules encountered, e.g., in plasmas containing more than one kind of multicharged ions. Naturally, the classical approach is well-suited for Rydberg quasimolecules.

Later applications of the results from [1.18, 1.19] included a magnetic stabilization of Rydberg quasimolecules [1.20], a problem of continuum lowering in plasmas (which plays a key role in calculations of the equation of state, partition function, bound-free opacities, and other collisional atomic transitions in plasmas) [1.21], and the study of the classical Stark effect for Rydberg quasi-molecules ([1.22] and section 2).

In these studies a particular attention was given to circular Rydberg states. Circular states of atomic and molecular systems are an important subject in its own right. They have been extensively studied both theoretically and experimentally for several reasons (see, e.g., [1.18-1.20, 1.24-1.37] and references therein): (a) they have long radiative lifetimes and highly anisotropic collision cross sections, thereby enabling experiments on inhibited spontaneous emission and cold Rydberg gases, (b) these classical states correspond to quantal coherent states, objects of fundamental importance, (c) a classical description of these states is the primary term in the quantal method based on the $1/n$-expansion, and (d) they can be used in developing atom chips.

As examples of experimental studies of Rydberg states, we refer to paper [1.23] where such studies made in the last three decades have been enumerated [1.23]. In particular, Day and Ebel [1.38] predicted theoretically in 1979 that probability of a wake electron being captured by fast-moving ions traversing a solid to a state with large principal (n) and angular momentum (l) quantum numbers is quite high and much of the time the electron is captured into circular Rydberg states ($l = n - 1$) distributed over a narrow band near n_{max}. Note here that $l = n - 1$ defines

circular orbits, whereas the full qualification of circular Rydberg states (CRS) requires $|m_l| = l = n - 1$. Day and Ebel proposed existence of an "optical window" in ion velocity as a possible explanation for non-observability of the CRS in beam-foil spectroscopy work. Also, the CRS are both long lived with respect to radiative transitions and short lived with respect to collisions, hence their observation requires a wide aperture and very good vacuum. Pegg *et al.*, in 1977 [1.39] observed a strong cascade tails in the decay curves of Cu^{18+} in a beam-foil interaction and attributed it to the successive decay of long-lived CRS or "yrast states". Note that CRS can radiate only to the next lower state, which leads to a chain of successive yrast transitions till they reach the ground state. Recently, from the study of the time-resolved beam-foil *X*-ray spectra of projectile or projectile-like ions of $2p$, $2s \rightarrow 1s$ transitions in H-like Fe, Ni, Cu, and Zn at different delay times (in the range 250-1600 ps). Nandi identified, in each case, a single circular Rydberg and/or an elliptic Rydberg state cascading successively to the $2p$ or $2s$ level.

Coming back to the ground-breaking theoretical papers [1.18, 1.19], it should be emphasized that the analysis there was not confined to circular orbits of the electron. Paper [1.19] presented a detailed study of *helical* Rydberg states of these diatomic Rydberg quasimolecules. For the stable motion, the electron trajectory was found to be a helix on the surface of a cone, with the axis coinciding with the internuclear axis. In this *helical* state, the electron, while spiraling on the surface of the cone, oscillates between two end-circles which result from cutting the cone by two parallel planes perpendicular to its axis (Fig. 1.1).

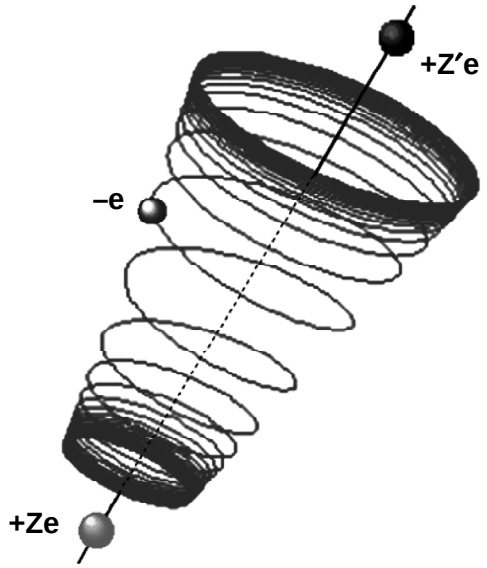

Figure 1.1: Sketch of the helical motion of the electron in the *ZeZ′*-system at the absence of the magnetic field. We stretched the trajectory along the internuclear axis to make its details better visible

Let us now reiterate how classical energy terms of diatomic Rydberg quasimolecules were obtained in paper [1.19]. (The meaning of "classical energy terms" is clarified below.) They were obtained by considering the Hamiltonian of the particle in a circular state in the cylindrical coordinates:

$$H = \frac{1}{2} p_\rho^2 + \frac{p_\varphi^2}{\rho^2} + p_z^2 - \frac{Z}{\sqrt{z^2 + \rho^2}} - \frac{Z'}{\sqrt{(R - z)^2 + \rho^2}} \tag{1.1}$$

where (ρ, φ, z) are the cylindrical coordinates with the z-axis being the internuclear axis and (p_ρ, p_φ, p_z) are the corresponding canonical momenta, Z and Z' are the charges at $z = 0$ and $z = R$. Since φ is cyclic, $p_\varphi = \text{const} = L$ and in the circular state $p_z = p_\rho = 0$, so (1.1), which is the particle energy, can be written as

$$E = \frac{L^2}{2\rho^2} - \frac{Z}{\sqrt{z^2 + \rho^2}} - \frac{Z'}{\sqrt{(R-z)^2 + \rho^2}} \tag{1.2}$$

which, using the scaled quantities defined below,

$$w = \frac{z}{R}, \quad v = \frac{\rho}{E}, \quad \ell = \frac{L}{\sqrt{ZR}}, \quad b = \frac{Z'}{Z}, \quad \varepsilon = -\frac{ER}{Z} \tag{1.3}$$

takes the form

$$\varepsilon = \frac{1}{\sqrt{w^2 + v^2}} + \frac{b}{\sqrt{(1-w)^2 + v^2}} - \frac{\ell^2}{2v^2} \tag{1.4}$$

In equilibrium, the derivatives of ε by both scaled coordinates (w, v) must vanish, so by taking the partial derivatives of (1.4) by each coordinate we obtain two more equations. The partial derivative of (1.4) by w set equal to zero yields

$$v^2 = \frac{w^{2/3}(1-w)^{4/3} - b^{2/3}w^2}{b^{2/3} - w^{2/3}(1-w)^{-2/3}} \tag{1.5}$$

and the partial derivative of (1.4) by v set equal to zero yields

$$\ell^2 = v^4 \left(\frac{1}{(w^2 + v^2)^{3/2}} + \frac{b}{((1-w)^2 + v^2)^{3/2}} \right) \tag{1.6}$$

Equation (1.5) determines the points (w, v) where the equilibrium is located. For $b > 1$, the equilibrium value of v exists for $0 < w < w_1$ and for $w_3 < w < 1$; for $b < 1$, it exists for $0 < w < w_3$ and $w_1 < w < 1$. Here we introduced the quantities $w_1 = 1/(1 + b^{1/2})$ and $w_3 = b/(1 + b)$. For definiteness, we shall consider the cases of $b > 1$ (or $Z' > Z$). There are no equilibrium points for $w < 0$ or $w > 1$ (i.e., for $z < 0$ or $z > R$): the z-component of the total Coulomb attraction force of the two centers has no balancing force at those points.

Solving (1.5) for v and substituting it into (1.6) and (1.4) and then solving (1.6) for ℓ and substituting it into (1.4), we obtain $\varepsilon(w, b)$-the scaled energy depending on the scaled internuclear coordinate w for a given ratio of the charges of the nuclei b.

If we scale the internuclear distance R as $r = (Z/L^2)R$, and given $\varepsilon = -ER/Z$ from (1.3), the energy of the electron can be represented in the form $E = -(Z^2/L^2)\varepsilon_1$, where we define $\varepsilon_1 = \varepsilon/r$. The scaling of E to ε_1 includes no more R and includes L, just like the scaling of R to r. Next, from the scaled quantities (1.3) we have $\ell^2 = L^2/(ZR)$ and from earlier in this paragraph, $r = ZR/L^2$, therefore, $r = 1/\ell^2$; with ℓ^2 taken from (1.6) and with v substituted from (1.5) we obtain $r(w, b)$. Thus, for any $L > 0$ and any $b > 0$, the dependence $\varepsilon_1(r)$, which represents the classical energy terms for this system, can be presented in a parametric form $\varepsilon(w, b)$, $r(w, b)$ via the parameter w for a given b. Here we give the explicit form of this dependence:

$$\varepsilon_1 = \left(\frac{1}{(w^2 + p)^{3/2}} + \frac{b}{((1-w)^2 + p)^{3/2}} \right) \left(\frac{w^2 + p/2}{(w^2 + p)^{3/2}} + \frac{b((1-w)^2 + p/2}{((1-w)^2 + p)^{3/2}} \right) \tag{1.7}$$

$$r = p^{-2} \left(\frac{1}{(w^2 + p)^{3/2}} + \frac{b}{((1-w)^2 + p)^{3/2}} \right)^{-1} \tag{1.8}$$

where we have defined the quantity p

$$p = v^2 = \frac{w^{2/3}(1-w)^{4/3} - b^{2/3}w^2}{b^{2/3} - w^{2/3}(1-w)^{-2/3}} \tag{1.9}$$

The plot of the energy terms given by (1.7) and (1.8) for b = 3 is given below. The same plot, with different ranges on both axes, is given in paper [1.19].

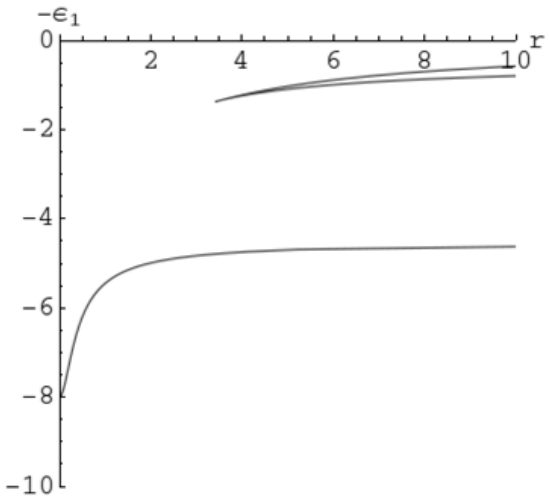

Figure 1.2: Classical energy terms: the dependence of the scaled classical energy ε_1 on the scaled internuclear distance r given by eq. (1.7) and (1.8) for b = 3

At this point it might be useful to clarify the relation between the classical energy terms $-\varepsilon_1(r)$ and the energy E. The former is a scaled quantity related to the energy as specified above:

$E = -(Z/L)^2 \varepsilon_1$. The projection L of the angular momentum on the internuclear axis is a *continuous* variable. The energy E depends on both ε_1 and L. Therefore, while the scaled quantity ε_1 takes a discrete set of values, the energy E takes a *continuous* set of values (as it should be in classical physics).

It turns out that the form of the parametric dependence can be significantly simplified and some of the properties of it can be found analytically by introducing a new parameter

$$\gamma = \left(\frac{1}{w} - 1\right)^{1/3} \tag{1.10}$$

In this case, $w = 0$ will correspond to $\gamma = +\infty$ and $w = 1$ will correspond to $\gamma = 0$, thus $\gamma > 0$ in the allowed regions. The points $w_1 = 1/(1 + b^{1/2})$ and $w_3 = b/(1 + b)$ defining the allowed regions $0 < w < w_1$, $w_3 < w < 1$ (here we assume $b > 1$) will correspond to $\gamma_1 = b^{1/6}$ and $\gamma_3 = 1/b^{1/3}$ (notice that $0 < w < w_1$ corresponds to $+\infty > \gamma > \gamma_1$ and $w_3 < w < 1$ corresponds to $\gamma_3 > \gamma > 0$). The energy terms $\varepsilon_1(r)$ will take the following parametric form:

$$\varepsilon_1(\gamma, b) = \frac{(b^{2/3} - \gamma^4)^2(\gamma(\gamma^3 - 2) + b^{2/3}(2\gamma^3 - 1))}{2(\gamma^3 - 1)^2(\gamma^6 - 1)} \tag{1.11}$$

$$r(\gamma, b) = \frac{\sqrt{b^{2/3}\gamma^2 - 1}(\gamma^6 - 1)^{3/2}}{\gamma(b^{2/3} - \gamma^4)^2} \tag{1.12}$$

The parametric plot of (1.11) and (1.12) with the parameter γ varied from 0 to $1/b^{1/3}$ and from $b^{1/6}$ to $+\infty$ for $b = 3$ will yield the same graph as in Fig. 1.2.

The crossing of the top two terms corresponds to the point where $r(\gamma, b)$ has a minimum or $\varepsilon_1(\gamma, b)$ has a maximum for a given b. Thus, taking the derivative of either function by γ and setting it equal to zero will yield a solution for the γ on the interval $\gamma > 1$ corresponding to the crossing. The equation for γ obtained from differentiating $r(\gamma)$ is a 6th-power polynomial and cannot be solved analytically; however, the equation for γ obtained from differentiating $\varepsilon_1(\gamma)$ can be solved analytically for γ. Below is the critical value γ_0 corresponding to the crossing.

$$\gamma_0 = \sqrt{b^{1/3} + \frac{(b-1)^{1/3}}{b^{1/6}}\left((\sqrt{b}+1)^{1/3} + (\sqrt{b}-1)^{1/3}\right)} \tag{1.13}$$

Substituting (1.13) into (1.12), we can obtain analytically the value of r corresponding to the crossing.

In the following chapters we consider the same system subjected to external potentials of various nature, as well as other configurations, such as a quasimolecule consisting of a proton, an electron and a muon. Atomic units ($\hbar = e = m_e = 1$) are used throughout the whole study.

2. ENHANCEMENT OF CHARGE EXCHANGE AND OF IONIZATION BY A STATIC ELECTRIC FIELD

2.1. Introduction

In papers [1.18, 1.20, 1.21] the study was focused at Circular Rydberg States (CRS) of the TCC system (the analysis in paper [1.19] went beyond CRS). CRS of atomic and molecular systems, with only one electron, correspond to $|m| = (n - 1) >> 1$, where n and m are the principal and magnetic electronic quantum numbers, respectively. They have been extensively studied [2.1-2.4] both theoretically and experimentally for several reasons listed in section 1.

While the authors of paper [1.20] studied analytically the effect of a magnetic field (along the internuclear axis) on CRS of the TCC system, in the present chapter we study the effect of an electric field (along the internuclear axis) on CRS of the TCC system. We provide analytical results for strong fields, as well as numerical results for moderate fields. We show that the electric field leads to the following consequences.

First, it leads to the appearance of an extra energy term: the fourth classical energy term - in addition to the three classical energy terms at zero field. Second, but more importantly, the electric field creates additional crossings of these energy terms. We show that some of these crossings enhance charge exchange while other crossings enhance the ionization of the Rydberg quasi-molecule.

2.2. Calculations of the Classical Stark Effect for a Rydberg Quasi-Molecule in a Circular State

We consider a TCC system, where the charge Z is at the origin and the Oz axis is directed to the charge Z', which is at $z = R$. A uniform electric field **F** is applied along the internuclear axis – in the negative direction of Oz axis. We study CRS where the electron moves around a circle in the plane perpendicular to the internuclear axis, the circle being centered at this axis.

Two quantities, the energy E and the projection L of the angular momentum on the internuclear axis are conserved in this configuration. We use cylindrical coordinates to write the equations for both.

$$E = \frac{1}{2}(\dot{\rho}^2 + \rho^2\dot{\varphi}^2 + \dot{z}^2) - \frac{Z}{r} - \frac{Z'}{r'} - Fz \tag{2.1}$$

$$L = \dot{\rho}^2\varphi \tag{2.2}$$

where ρ is the distance of the electron from the internuclear axis, φ is its azimuthal angle, z is the projection of the radius-vector of the electron on the internuclear axis, r and r' are the distances of the electron from the particle to Z and Z', respectively.

The circular motion implies that $d\rho/dt = 0$; as the motion occurs in the plane perpendicular to the z-axis, $dz/dt = 0$. Further, expressing r and r' through ρ and z, and taking $d\varphi/dt$ from (2.2), we have:

$$E = \frac{L^2}{2\rho^2} - \frac{Z}{\sqrt{\rho^2 + z^2}} - \frac{Z'}{\sqrt{\rho^2 + (R - z)^2}} - Fz \tag{2.3}$$

With the scaled quantities

$$w = \frac{z}{R}, \quad v = \frac{\rho}{R}, \quad b = \frac{Z'}{Z}, \quad \varepsilon = -\frac{ER}{Z}, \quad \ell = \frac{L}{\sqrt{ZR}}, \quad f = \frac{FR^2}{Z}, \quad r = \frac{ZR}{L^2} \tag{2.4}$$

our energy equation takes the form below:

$$\varepsilon = \frac{1}{\sqrt{w^2 + v^2}} + \frac{b}{\sqrt{(1 - w)^2 + v^2}} + fw - \frac{\ell^2}{2v^2} \tag{2.5}$$

We can seek the equilibrium points by finding partial derivatives of ε by the scaled coordinates w, v and setting them equal to zero. This will give the following two equations.

$$f + \frac{b(1 - w)}{((1 - w)^2 + v^2)^{3/2}} = \frac{w}{(w^2 + v^2)^{3/2}} \tag{2.6}$$

$$\ell^2 = v^4 \left(\frac{1}{(w^2 + v^2)^{3/2}} + \frac{b}{((1 - w)^2 + v^2)^{3/2}} \right) \tag{2.7}$$

From the definitions of the scaled quantities (4), $\ell^2 = 1/r$ and $E = -(Z/R)\varepsilon$. Since $r = ZR/L^2$,

$E = -(Z/L)^2 \varepsilon/r$, where $r = 1/\ell^2$ can be obtained by solving (2.7) for ℓ. Substituting ℓ into the energy equation, we get the three master equations for this configuration.

$$\varepsilon_1 = p^2 \left(\frac{1}{(w^2 + p)^{3/2}} + \frac{b}{((1 - w)^2 + p)^{3/2}} \right) \left(\frac{w^2 + p/2}{(w^2 + p)^{3/2}} + \frac{b((1 - w)^2 + p/2}{((1 - w)^2 + p)^{3/2}} + fw \right) \tag{2.8}$$

$$r = p^{-2} \left(\frac{1}{(w^2 + p)^{3/2}} + \frac{b}{((1 - w)^2 + p)^{3/2}} \right)^{-1} \tag{2.9}$$

$$f + \frac{b(1 - w)}{((1 - w)^2 + p)^{3/2}} = \frac{w}{(w^2 + p)^{3/2}} \tag{2.10}$$

where $E = -(Z/L)^2 \varepsilon_1$ and $p = v^2$. Thus, ε_1 is the "true" scaled energy, whose equation for E does not include R. The scaled energy ε_1 and internuclear distance r in (2.8) and (2.9) now explicitly depend only on the coordinates w and p (besides the constants b and f). Therefore, if we solve (2.10) for p and substitute it into (2.8) and (2.9), we will have the parametric solution $\varepsilon_1(r)$ with the parameter w.

Our focus is at crossings of energy terms of the *same symmetry*. In the quantum TCC problem, "terms of the same symmetry" means terms of the same magnetic quantum number m [1.8 – 1.11]. Therefore, in our classical TCC problem, we fixed the angular momentum projection L and study the behavior of the classical energy at $L = \text{const} \geq 0$ (the results for L and $-L$ are physically the same).

Equation (2.10) does not allow an exact analytical solution for p. Therefore, we will use an approximate analytical method.

Figure 2.1 shows a contour plot of (2.10) for a relatively weak field $f = 0.3$ at $b = 3$, with w on the horizontal axis and p on the vertical. The plot has two branches. The left branch spans from $w = 0$ to $w = w_1$. The right one actually has a small two-valued region between some $w = w_3$ and 1 ($w_3 < 1$). Indeed, at $w = 1$, there are two values of p: $p = 0$ and $p = f^{-2/3} - 1$. Thus, the two-valued region exists only for $f < 1$.

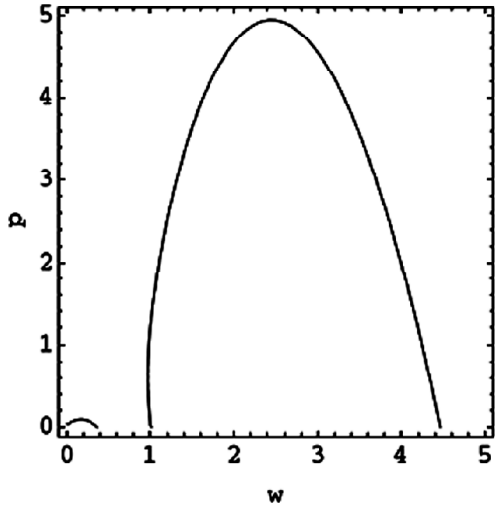

Figure 2.1: Contour plot of (2.10) for a relatively weak field $f = FR^2/Z = 0.3$ at $b = Z'/Z = 3$

The right branch touches the abscissa at $w = 1$ and at some $w = w_2$. Analytical expressions for w_1 and w_2 are given in Appendix 2A. The quantity w_3 is a solution of the equation

$$f^{2/5}(2w_3 - 1)^{3/5} = w_3^{2/5} - b^{2/5}(1 - w_3)^{2/5} \tag{2.11}$$

The method, by which w_3 was found from (2.11), is presented in Appendix 2B.

Figure 2 shows a contour plot of (2.10) for a relatively strong field $f = 20$ at $b = 3$. It is seen that there is no two-valued region.

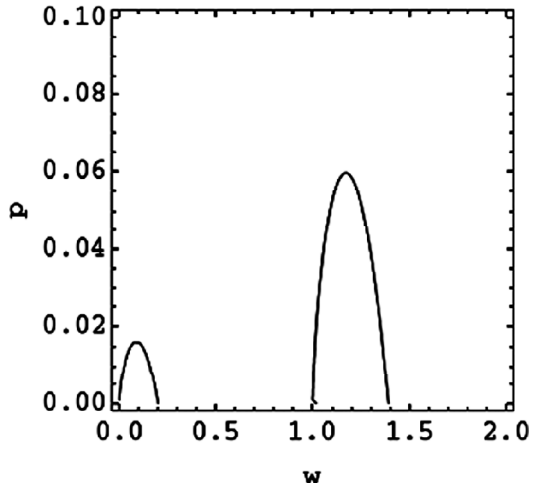

Figure 2.2: The same as in Fig. 2.1, but for a relatively strong field $f = FR^2/Z = 20$

From now on we consider the situation where the radius of the electronic orbit is relatively small, meaning that $p << 1$. Physically this corresponds to strong fields $f > f_{min} \sim 10$.

Solving (2.10) in the small-p approximation, we obtain

$$p = \left(\frac{w}{f + \dfrac{b}{(1-w)^2}} \right)^{2/3} - w^2 \tag{2.12}$$

for the left branch ($0 < w < w_1$) and

$$p = \left(\frac{b(1-w)}{\dfrac{1}{w^2} - f} \right)^{2/3} - (1-w)^2 \tag{2.13}$$

for the right branch ($1 < w < w_2$). Substituting these results into (2.8) and (2.9), we get approximate solutions for energy terms $-\varepsilon_1(r)$ in both regions in a parametric form, w being the parameter. Now we plot classical energy terms $-\varepsilon_1(r)$ by varying the parameter w over both regions, using the appropriate formula for each one.

Figure 2.3 shows classical energy terms at $b = 3$ for $f = 20$. Figure 2.4 presents classical energy terms at $b = 3$ for $f = 5$.

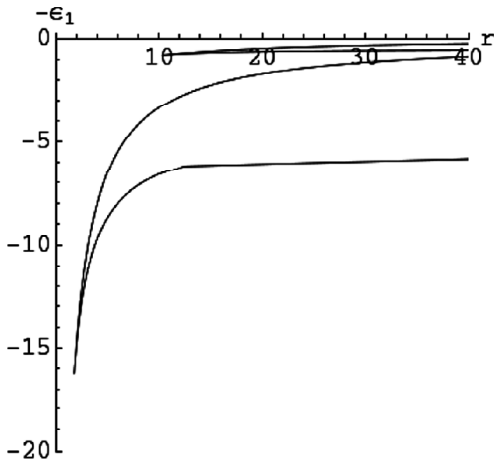

Figure 2.3: Classical energy terms at $b = 3$ for $f = 20$

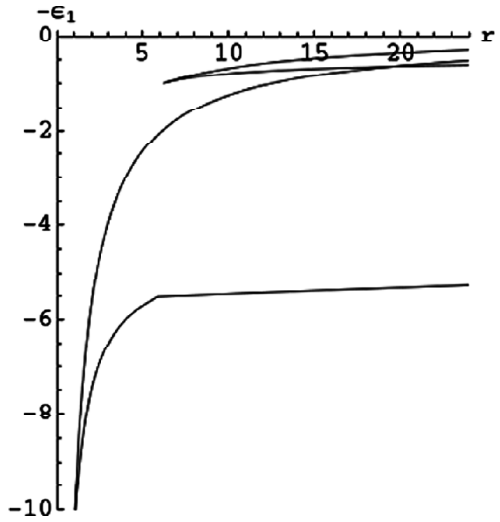

Figure 2.4: Classical energy terms at $b = 3$ for $f = 5$

We also solved the same problem numerically. By comparison we found that the approximate analytical solution is accurate for fields $f = 5$ and above.

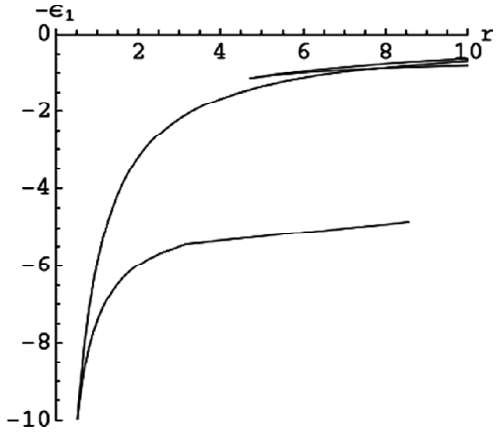

Figure 2.5: Classical energy terms at $b = 3$ for $f = 2$

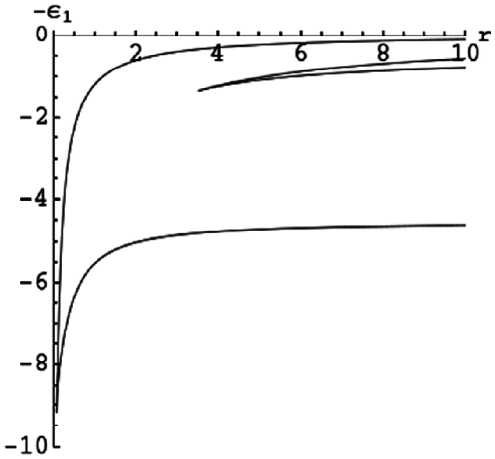

Figure 2.6: Classical energy terms at $b = 3$ for $f = 0.1$

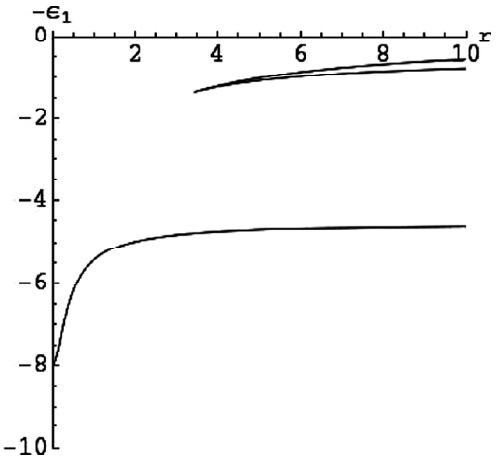

Figure 2.7: Classical energy terms at $b = 3$ at the absence of the electric field

Figures 2.5 and 2.6 show the numerically obtained classical energy terms at $b = 3$ for $f = 2$ and $f = 0.1$, respectively. For comparison, Fig. 2.7 shows the classical energy terms at $b = 3$ at the absence of the electric field (it had been previously presented in papers [1.18, 1.19] and is the same as Fig. 1.2).

The electric field causes several important new features compared to the zero-field case. While at $f = 0$ there are three classical energy terms, the electric field brings up the fourth classical energy term. Indeed, let us take as an example the case of $f = 5$ at $b = 3$ presented in Fig. 2.4. There are four energy terms that we label as follows:

#1 – the lowest term;

#2 – the next term up (which has a *V*-type crossing with term 1);

#3 – the next term up;

#4 – the highest term (which has a *V*-type crossing with term 3).

We will use this labeling also while discussing all other plots (except the plot in Fig. 2.7 for $f = 0$): terms 1 and 2 will be those having the *V*-type crossing at the lower energy, terms 3 and 4 will be those having the *V*-type crossing at the higher energy, At $f = 0$ term 2 is absent, but it appears at any non-zero value of f – no matter how small. Actually, as f approaches zero, this term behaves like $-f/r$, which is why it disappears at $f = 0$.

The existence of this additional term can be explained physically as follows. When $f = 0$, equilibrium of the orbital plane to the right of Z' (i.e., for $w > 1$) does not exist, so that the values of w_1 and w_3 reduce to the ones presented in papers [1.18, 1.19] and the right branch of $p(w)$ asymptotically goes to infinity when w goes down to w_3. When an infinitesimal field f appears, the right branch flips over positive infinity and ends up on the abscissa at $w_2 \to \infty$, thus enabling the whole region $w > 1$ for equilibrium. As the field grows, w_2 decreases. Physically, the force from the electric field at $w > 1$ balances out the Coulomb attraction of the $Z - Z'$ system on the left – the situation not possible for $f = 0$. This term is obtained by varying the parameter w from 1 to w_2.

We emphasize that the above examples presented for $Z'/Z = 3$ represent a typical situation. In fact, for any pair of Z and $Z' \neq Z$, at the presence of the electric field, there are four classical energy terms of the same symmetry for CRS.

Another important new feature caused by the electric field is *X*-type crossings of the classical energy terms. This kind of crossings and their physical consequences are discussed in the next section.

2.3. *X*-Type Crossings of Classical Energy Terms and Their Physical Consequences

Figure 2.8 shows a magnified version of the energy terms 2, 3, and 4 at $b = 3$ for $f = 2$. Figure 2.9 shows a further magnified version of the energy terms 2 and 4 at $b = 3$ for $f = 2$. Compared to Fig. 2.5 for the same b and f, in Figs. 2.8 and 2.9 we decreased the exhibited energy range, but increased the exhibited range of the internuclear distances r.

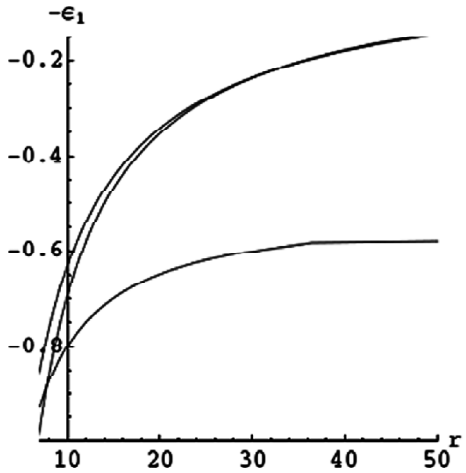

Figure 2.8: Magnified plot of the classical energy terms 2, 3, and 4 at $b = 3$ for $f = 2$

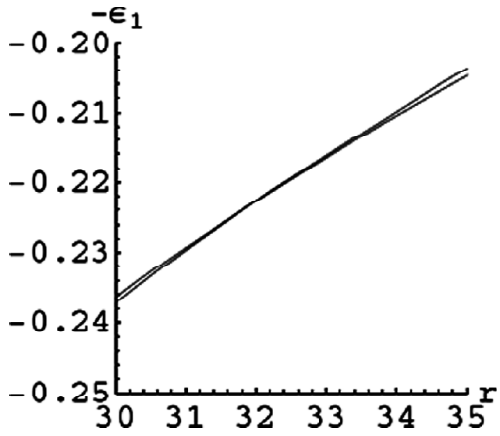

Figure 2.9: Further magnified plot of the classical energy terms 2 and 4 at $b = 3$ for $f = 2$

It is seen that term 2 has the *X*-type crossing with term 3 at $r = 7.8$ and the *X*-type crossing with term 4 at $r = 32$. The situation where there are two *X*-type crossings exists in a limited range of the electric fields. For example, for $b = 3$:

- two *X*-type crossings exist at $1.31 < f < 2.4$;
- there are no *X*-type crossings at $f < 1.31$;
- there is one *X*-type crossing at $f > 2.4$ (the crossing of terms 2 and 3).

To reveal physical consequences of the *X*-type crossings, let us first discuss the origin of all four classical energy terms for arbitrary $Z'/Z \neq 1$. At $r \to \infty$, term 3 corresponds to the energy of a hydrogenlike ion of the nuclear charge $Z_{min} = \min(Z', Z)$, slightly perturbed by the charge $Z_{max} = \max(Z', Z)$, as shown in [1.18, 1.19].

At $r \to \infty$, term 4 corresponds to a near-zero-energy state (where the electron is almost free), as shown in [1.18, 1.19]. If the ratio Z'/Z is of the order of (but not equal to) unity, this term at $r \to \infty$ can be described only in the terminology of elliptical coordinates (rather than parabolic or spherical coordinates), meaning that even at $r \to \infty$ the electron is shared between the *Z*- and *Z′*-centers. However, in the case of $Z' >> Z$, this term can be asymptotically considered as the *Z′*-term, as shown in [1.18, 1.19]. It has the *V*-type crossing with term 3, which asymptotically is the *Z*-term (since $Z_{min} = Z$ for $Z' > Z$). Likewise, in the case of $Z' << Z$, term 4 can be asymptotically considered as the *Z*-term, as shown in [1.18, 1.19]. It has the *V*-type crossing with term 3, which asymptotically is the *Z′*-term (since $Z_{min} = Z'$ for $Z' < Z$).

At $r \to \infty$, term 1 corresponds to the energy of a hydrogenlike ion of the nuclear charge Z_{max} slightly perturbed by the charge Z_{min}, as shown in [1.18, 1.19]. As for the term 2, at $r \to \infty$ it has properties similar to term 4, but with the interchange of Z_{max} and Z_{min}. In particular, in the case of $Z' >> Z$, this term can be asymptotically considered as the *Z*-term, having the *V*-type crossing with term 1, which asymptotically is the *Z′*-term (since $Z_{max} = Z'$ for $Z' > Z$). In the case of $Z' << Z$, term 2 can be asymptotically considered as the *Z′*-term, having the *V*-type crossing with term 1, which asymptotically is the *Z*-term (since $Z_{max} = Z$ for $Z' < Z$).

Thus, when *Z* and *Z′* differ significantly from each other, the *V*-type crossings occur between two classical energy terms that can be asymptotically labeled as *Z*- and *Z′*-terms. This situation *classically depicts charge exchange*, as explained in papers [1.18, 1.19]. Indeed, say, initially at $r \to \infty$, the electron was a part of the hydrogenlike ion of the nuclear charge Z_{min}. As the charges *Z* and *Z′* come relatively close to each other, the two terms undergo a *V*-type crossing and the electron is shared between the *Z*- and *Z′*-centers. Finally, as the charges *Z* and *Z′* go away from each other, the electron ends up as a part of the hydrogenlike ion of the nuclear charge Z_{max}.

So, the first distinction caused by the electric field is an additional, second *V*-type crossing leading to charge exchange – compared to the zero-field case where there was only one such crossing. However, the second *V*-type crossing (the crossing of terms 1 and 2) occurs at the internuclear distance $r_{V_2} << r_{V_1}$, where r_{V_1} is the internuclear distance of the first *V*-type crossing (the crossing of terms 3 and 4). Therefore the cross-section of the charge

exchange corresponding to the second *V*-type crossing is much smaller than the corresponding cross-section for the first *V*-type crossing.

Now let us discuss the *X*-type crossing from the same point of view. When *Z* and *Z*′differ significantly from each other, the *X*-type crossing of terms 2 and 4 is the crossing of terms that can be asymptotically labeled as *Z*- and *Z*′-terms. Thus, this situation again *classically depicts charge exchange*. The most important is that this crossing occurs at the internuclear distance $r_{X_1} >> r_{V_1} >> r_{V_2}$. Therefore, the cross-section of charge exchange due to this *X*-type crossing is much greater than the corresponding cross-sections of for the *V*-type crossings. This is the most fundamental physical consequence caused by the electric field: a *significant enhancement of charge exchange*.

When *Z* and *Z*′-differ significantly from each other, the *X*-type crossing of terms 2 and 3 is the crossing of terms having the same asymptotic labeling: either both of them are *Z*-terms or both of them are *Z*′-terms. Therefore this second *X*-type crossing (at $r = r_{X_2}$) does not correspond to charge exchange – rather it represents an *additional ionization channel*. Indeed, say, initially at $r \to \infty$, the electron resided on term 3 of the hydrogenlike ion of the nuclear charge *Z*. As the distance between the charges *Z* and *Z*′ decreases to $r = r_{X_2}$, the electron can switch to term 2, which asymptotically corresponds to a near-zero-energy state (of the same hydrogenlike ion of the nuclear charge *Z*) where the electron would be almost free. So, as the charges *Z* and *Z*′ go away from each other, the system undergoes the ionization. Thus, another physical consequence caused by the electric field is the appearance of the additional ionization channel. This should have been expected since the electric field promotes the ionization of atomic and molecular systems.

2.4. Conclusions

We studied the effect of an electric field (along the internuclear axis) on circular Rydberg states of the two Coulomb centers system. We provided analytical results for strong fields, as well as numerical results for moderate fields. We showed that the electric field had the following effects.

The first effect is the appearance of an extra energy term: the *fourth classical energy term* – in addition to the three classical energy terms at zero field. This term exhibits a *V*-type crossing with the lowest energy term. The two highest energy terms continue having a *V*-type crossing like at the zero field. In the situation where the charges *Z*′differ significantly from each other, both *V*-type crossings correspond to charge exchange.

The second effect is the appearance of a new type of crossings – *X*-type crossings. One of the *X*-type crossings (existing in a limited range of the electric field strength) corresponds to charge exchange at a much larger internuclear distance compared to the *V*-type crossings. Therefore the cross-section of charge exchange due to this *X*-type crossing is much greater than the cross-section of charge exchange due to *V*-type crossings. Thus, the electric field can *significantly enhance charge exchange*. We believe that this is the most important result of the present chapter.

The other *X*-type crossing does not correspond to charge exchange. Instead, it represents an *additional ionization channel*.

APPENDIX 2A
THE LIMITS w_1 AND w_2 ON THE GRAPH OF $p(w)$ IN Eq. (2.10)

The analytical results for the quantities w_1 and w_2, obtained using the software Mathematica, have the following form.

For w_1:

$$w_1 = \frac{\sqrt{3}}{6}\left(\sqrt{3} - \sqrt{\frac{(b+f-1)^2}{a_1 f} + \frac{a_1}{f} - \frac{2(b+f-1)}{f} + 3} + \right.$$

$$\left. + \sqrt{\frac{6\sqrt{3}(b+1)}{f\sqrt{\frac{(b+f-1)^2}{a_1 f} + \frac{a_1}{f} - \frac{2(b+f-1)}{f} + 3}} - \frac{(b+f-1)^2}{a_1 f} - \frac{a_1}{f} - \frac{4(b+f-1)}{f} + 6}\right)$$

where

$$a_1 = \sqrt[3]{54\,bf + (b + f - 1)^3 + 6\sqrt{3bf}\sqrt{b^3 + 3b^2(f-1) + (f-1)^3 + 3b(1 + f(f+7))}}$$

For w_2:

$$w_2 = \frac{\sqrt{3}}{6}\left(\sqrt{3} + \sqrt{\frac{(b-f+1)^2}{a_2 f} + \frac{a_2}{f} + \frac{2(b+1)}{f} + 1} + \right.$$
$$\left. + \sqrt{\frac{6\sqrt{3}(b-1)}{f\sqrt{\frac{(b-f+1)^2}{a_2 f} + \frac{a_2}{f} + \frac{2(b+1)}{f} + 1}} - \frac{(b-f+1)^2}{a_2 f} - \frac{a_2}{f} + \frac{4(b+1)}{f} + 2}\right)$$

where

$$a_2 = \sqrt[3]{(f-1)^3 + 3b^2(f-1) - b^3 - 3b(1 + f(f+16)) + 6\sqrt{3bf}\sqrt{(b+1)^3 - 3f(1 + b(b-7)) + 3f^2(b+1) - f^3}}$$

APPENDIX 2B
FINDING THE LOWER LIMIT w_3 OF THE TWO-VALUED REGION ON THE GRAPH OF $p(w)$ IN Eq. (2.10)

Defining a function

$$F(p, w) = f + \frac{b(1-w)}{((1-w)^2 + p)^{3/2}} - \frac{w}{(w^2 + p)^{3/2}}, \tag{2.B.1}$$

we can rewrite (2.10) as $F(p, w) = 0$. From the graph it is seen that at w_3, $dw/dp = 0$. Since $F(p, w) = 0$, $dF/dp = 0$ as well. On the other hand, $F(w, p) = F(w(p), p) = 0$ and

$$\frac{dF}{dp} = \frac{\partial F}{\partial w}\frac{dw}{dp} + \frac{\partial F}{\partial p} = 0 \tag{2.B.2}$$

from where we get

$$\frac{dw}{dp} = -\frac{\partial F/\partial p}{\partial F/\partial w} \tag{2.B.3}$$

Setting the right side of (2.B.1) and (2.B.3) to zero, we obtain the system of two equations, solving which for w will give us the point on the contour plot of $F(p, w) = 0$ where the derivative dw/dp vanishes, i.e., the desired point. Excluding p from the system, we reduce the equation to

$$f^{2/5}(2w_3 - 1)^{3/5} = w_3^{2/5} - b^{2/5}(1 - w_3)^{2/5} \tag{2.B.4}$$

where w was renamed to w_3 for clarity. This is (2.11) of this chapter.

3. EFFECT OF PLASMA SCREENING ON CIRCULAR STATES OF DIATOMIC RYDBERG QUASIMOLECULES AND THEIR APPLICATION TO CONTINUUM LOWERING IN PLASMAS

3.1. Introduction

In the previous chapters we studied analytically CRS of the two-Coulomb-center system, the system (denoted as ZeZ') consisting of two nuclei of charges Z and Z', separated by a distance R, and one electron – see also [1.18 – 1.20, 1.24, 1.25, 1.34, 3.1]. Energy terms of these Rydberg quasimolecules were obtained for a field-free case, as well as under an electric field or under a magnetic field.

The Rydberg quasimolecules of this type naturally occur in high density plasmas of several types of ions, where a fully-stripped ion of the charge Z' is in the proximity of a hydrogenlike ion of the nuclear charge Z (or where a fully-stripped ion of the charge Z is in the proximity of a hydrogenlike ion of the nuclear charge Z'). Therefore in the present chapter we study the effects of plasma screening on CRS of these Rydberg quasimolecules – the effects not taken into account in the previous works. We provide analytical results for weak screening, as well as numerical results for moderate and strong screening. We show that the screening leads to the following consequences.

The screening causes an additional energy term to appear – compared to the absence of the screening. This new term has a *V*-type crossing with the lowest energy term. The internuclear potential is also affected by the screening, destabilizing the nuclear motion for $Z > 1$ and stabilizing it for $Z = 1$.

We also study the effect of plasma screening on continuum lowering (CL) in the ionization channel. CL was studied for over 50 years – see, e.g., books/reviews [3.2 – 3.6] and references therein. Calculations of CL evolved from ion sphere models to dicenter models of the plasma state [3.4, 3.7 – 3.12]. One of such theories – a percolation theory [3.4, 3.9] – calculated CL defined as an absolute value of energy at which an electron becomes bound to a macroscopic portion of plasma ions (a quasi-ionization). In 2001 the value of CL in the ionization channel was derived analytically, which was disregarded in the percolation theory: a quasimolecule, consisting of the two ion centers plus an electron, can get ionized in a true sense of this word before the electron would be shared by more than two ions [1.21]. It was also shown in [1.21] that, whether the electron is bound primarily by the smaller or by the larger out of two positive charges Z and Z', makes a dramatic qualitative and quantitative difference for this ionization channel. The results in [1.21] were obtained for circular states of the corresponding Rydberg quasimolecules.

In the present chapter we show that the screening decreases CL in the ionization channel, making CL vanish as the screening factor increases.

3.2. Calculation of the Effect of Plasma Screening and Classical Energy Terms for a Rydberg Quasimolecule in a Circular State

Plasma screening of a test charge is a well-known phenomenon. For a hydrogen atom or a hydrogen-like ion (an H-atom, for short), it is effected by replacing the pure Coulomb potential by a screened Coulomb potential which contains a physical parameter – the screening length a. For example, the Debye-Hückel (or Debye) interaction of an electron with the electronic shielded field of an ion of charge Z is $U(R) = -(Ze^2/R) \exp(-R/a)$, where $a = (kT/(4\pi e^2 N_e))^{1/2} \approx 1.304 \times 10^4 (10^{10}/N_e)^{1/2} T^{1/2} a_0$, where N_e (cm^{-3}) and T (K) are the electron density and temperature, respectively.

We study a two-Coulomb center (TCC) system with the charge Z placed at the origin, and the Oz axis is directed at the charge Z', which is at $z = R$, the system being submerged in a plasma of a screening length a. We consider the circular orbits of the electron which are perpendicular to the internuclear axis and centered on the axis.

Two quantities, the energy E and the projection L of the angular momentum on the internuclear axis are conserved in this configuration. We use cylindrical coordinates to write the equations for both:

$$E = \frac{1}{2}(\dot{\rho}^2 + \rho^2\dot{\varphi}^2 + \dot{z}^2) - \frac{Z}{r}e^{-r/a} - \frac{Z'}{r'}e^{-r'/a} \tag{3.1}$$

$$L = \rho^2 \varphi \tag{3.2}$$

where r and r' are distances from the electron to Z and Z'. The circular motion implies that $d\rho/dt = 0$; as the motion occurs in the plane perpendicular to the z-axis, $dz/dt = 0$. Further, expressing r and r' through ρ and z, and taking $d\varphi/dt$ from (3.2), we have:

$$E = \frac{L^2}{2\rho^2} - \frac{Z}{\sqrt{\rho^2 + z^2}} e^{-\sqrt{\rho^2 + z^2}/a} - \frac{Z'}{\sqrt{\rho^2 + (R-z)^2}} e^{-\sqrt{\rho^2 + (R-z)^2}/a} \tag{3.3}$$

With the scaled quantities

$$w = \frac{z}{R}, \quad p = \left(\frac{\rho}{R}\right)^2, \quad b = \frac{Z'}{Z}, \quad \varepsilon = -\frac{ER}{Z}, \quad \ell = \frac{L}{\sqrt{ZR}}, \quad \lambda = \frac{R}{a}, \quad r = \frac{ZR}{L^2} \tag{3.4}$$

our energy equation takes the form below:

$$\varepsilon = \frac{e^{-\lambda\sqrt{w^2 + p}}}{\sqrt{w^2 + p}} + \frac{be^{-\lambda\sqrt{(1-w)^2 + p}}}{\sqrt{(1-w)^2 + p}} - \frac{\ell^2}{2p} \tag{3.5}$$

We can seek the equilibrium points by finding partial derivatives of ε by the scaled coordinates w, p and setting them equal to zero. This will give the following two equations.

$$\frac{we^{-\lambda\sqrt{w^2 + p}}}{w^2 + p}\left(\frac{1}{\sqrt{w^2 + p}} + \lambda\right) = \frac{b(1-w)e^{-\lambda\sqrt{(1-w)^2 + p}}}{(1-w)^2 + p}\left(\frac{1}{\sqrt{(1-w)^2 + p}} + \lambda\right) \tag{3.6}$$

$$\frac{\ell^2}{p^2} = \frac{e^{-\lambda\sqrt{w^2 + p}}}{w^2 + p}\left(\frac{1}{\sqrt{w^2 + p}} + \lambda\right) + \frac{be^{-\lambda\sqrt{(1-w)^2 + p}}}{(1-w)^2 + p}\left(\frac{1}{\sqrt{(1-w)^2 + p}} + \lambda\right) \tag{3.7}$$

From the definitions of the scaled quantities (3.4), $\ell^2 = 1/r$ and $E = -(Z/R)\varepsilon$. Since $r = ZR/L^2$, $E = -(Z/L)^2 \varepsilon/r$, where $r = 1/\ell^2$ can be obtained by solving (3.7) for ℓ. Thus, the scaled energy without explicit dependence on R is ε/r, which we shall denote ε_1. Using this, equations (3.5), (3.6) and (3.7) can be transformed into the following three master equations for this configuration.

$$\varepsilon_1 = \left(\frac{p(1 + \lambda\sqrt{w^2 + p})e^{-\lambda\sqrt{w^2 + p}}}{(1-w)(w^2 + p)^{3/2}}\right)^2 \left(\frac{(1-w)(w^2 + p)}{1 + \lambda\sqrt{w^2 + p}} + \frac{w((1-w)^2 + p)}{1 + \lambda\sqrt{(1-w)^2 + p}} - \frac{p}{2}\right) \tag{3.8}$$

$$r = \frac{(1-w)(w^2 + p)^{3/2} e^{\lambda\sqrt{w^2 + p}}}{p^2(1 + \lambda\sqrt{w^2 + p})} \tag{3.9}$$

$$\frac{w(1 + \lambda\sqrt{w^2 + p})e^{-\lambda\sqrt{w^2 + p}}}{(w^2 + p)^{3/2}} = \frac{b(1-w)(1 + \lambda\sqrt{(1-w)^2 + p})e^{-\lambda\sqrt{(1-w)^2 + p}}}{((1-w)^2 + p)^{3/2}} \tag{3.10}$$

The quantities ε_1 and r now depend only on the coordinates w and p (besides the constant λ). Therefore, if we resolve (3.10) for p and substitute it to (3.8) and (3.9), we obtain the parametric solution for the energy terms $\varepsilon_1(r)$ with the parameter w for the given b and λ.

Equation (3.10) does not allow an exact analytical solution for p. Therefore, we will use an approximate analytical method.

Below is the contour plot of this equation for $b = 3$ and $\lambda = 0.1$.

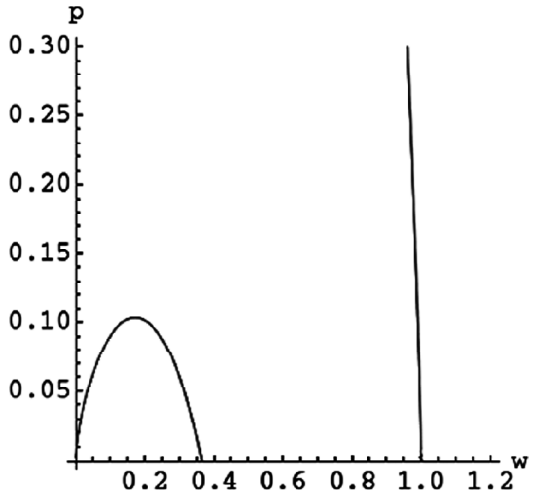

Figure 3.1: Contour plot of equation (3.10) for $b = 3$ and $\lambda = 0.1$

As in [1.19] and Section 2, the plot has two branches, the left one spanning from $w = 0$ to $w = w_1$, and the right one from the asymptote $w = w_3$ to $w = 1$. w_1 is a solution of the equation

$$(1-w_1)^2(1+\lambda w_1)e^{\lambda(1-2w_1)} = bw_1^2(1+\lambda(1-2w_1)) \tag{3.11}$$

in the interval $0 < w_1 < 1$, and w_3 does not depend on λ and equals $b/(1 + b)$ – the same as in [1.19] for $\lambda = 0$ – the "default" case described in Section 1. As λ increases, w_1 and the p-coordinate of the maximum of the left branch increase, but the general shape of both curves is preserved. Below is the plot for a relatively strong $\lambda = 2$.

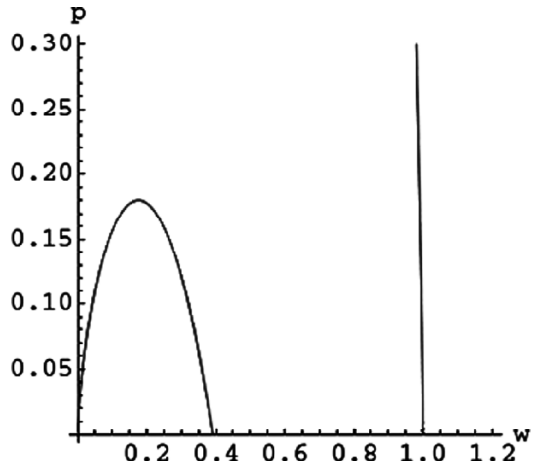

Figure 3.2: Contour plot of equation (3.10) for $b = 3$ and $\lambda = 2$

An approximation was made for small values of λ. Approximating (3.10) in the first power of λ, we obtain the expression involving only the second and higher powers of λ. Therefore, an attempt was made using the value of $p(w)$ for $\lambda = 0$ presented in [1.19], which we shall denote as p_0; it is the same as the quantity in (1.5). Further, taking the higher powers of λ into account, we obtained the next-order approximation for $p(w)$:

$$p(w) = p_0 + \frac{\lambda^2}{6}(1-w)\left(1+(1-2w)\left(\frac{w^{2/3}+b^{2/3}(1-w)^{2/3}}{w^{2/3}-b^{2/3}(1-w)^{2/3}}\right)^2\right) \tag{3.12}$$

where

$$p_0 = \frac{w^{2/3}(1-w)^{4/3} - b^{2/3}w^2}{b^{2/3} - w^{2/3}(1-w)^{-2/3}} \tag{3.13}$$

the zero-λ value as in (1.5).

Equation (3.11) can be approximated by substituting $1 + \lambda(1 - 2w_1)$ in place of $\exp(\lambda(1 - 2w_1))$, which will render it a 4th-degree polynomial in w_1. The analytical expression for it is given in Appendix 3.A.

Substituting (3.12) into (3.8) and (3.9), we obtain the approximate parametric solution for the energy terms $-\varepsilon_1(r)$ by running the parameter w on $0 < w < w_1$ and $w_3 < w < 1$. Empirically, by comparison with the numerical results, it was found that using the value of p from (3.13) on the $0 < w < w_1$ range and from (3.12) on the $w_3 < w < 1$ range gives the best approximate results. Below are the approximate terms for $b = 3$ and different values of λ.

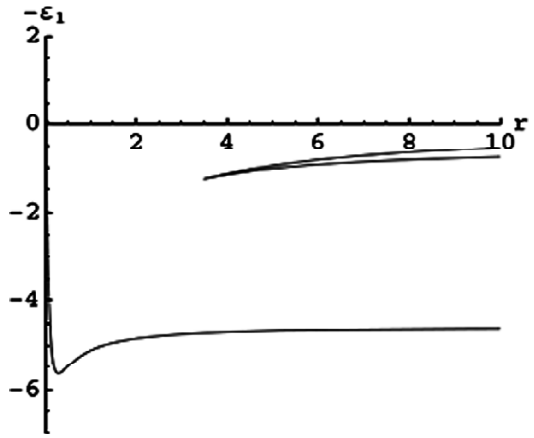

Figure 3.3: Approximate classical energy terms for $b = 3$ at $\lambda = 0.1$

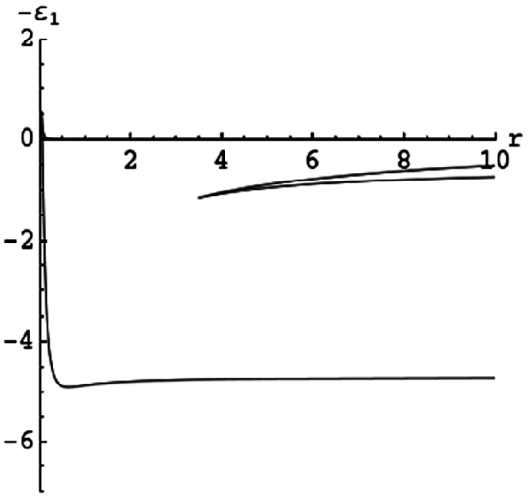

Figure 3.4: Approximate classical energy terms for $b = 3$ at $\lambda = 0.2$

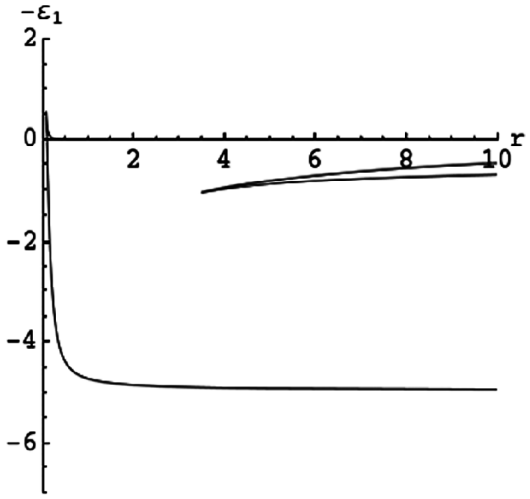

Figure 3.5: Approximate classical energy terms for b = 3 at λ = 0.3

A numerical solution has also been made. It confirmed that the analytical solution was a good approximation for $\lambda < 0.3$. Below are the terms plotted for selected arbitrary values of λ.

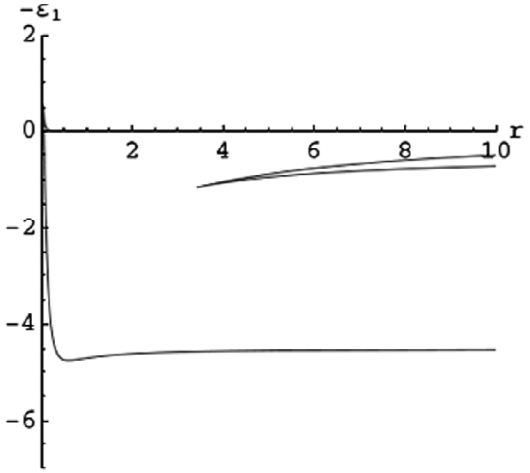

Figure 3.6: Numerical classical energy terms for b = 3 at λ = 0.2

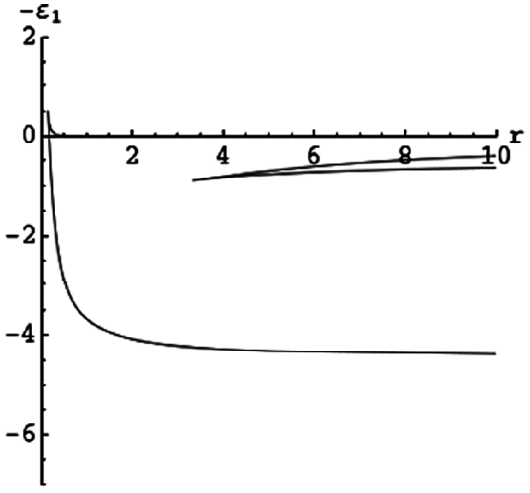

Figure 3.7: Numerical classical energy terms for b = 3 at λ = 0.5

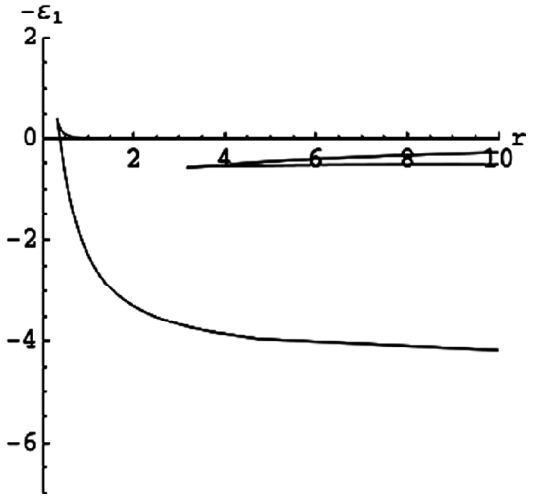

Figure 3.8: Numerical classical energy terms for $b = 3$ at $\lambda = 1$

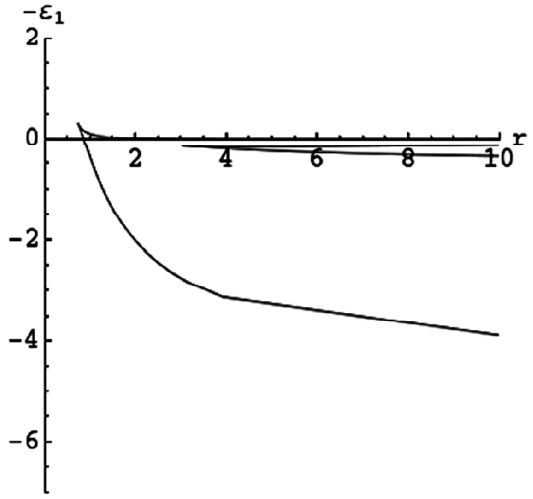

Figure 3.9: Numerical classical energy terms for $b = 3$ at $\lambda = 2$

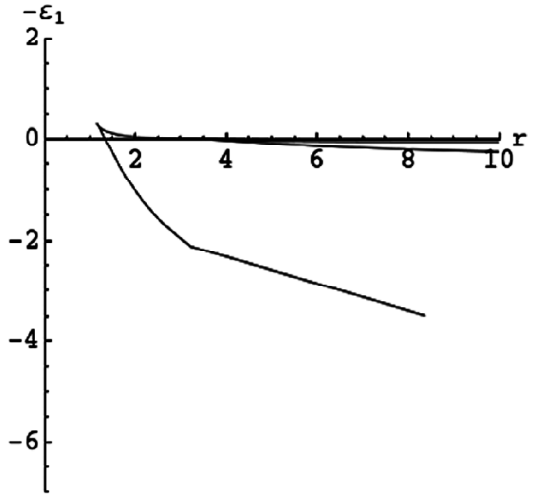

Figure 3.10: Numerical classical energy terms for $b = 3$ at $\lambda = 3$

The following reminder should be made. The above plots represent "classical energy terms" of the same symmetry. (In physics of diatomic molecules, the terminology "energy terms of the same symmetry" means the energy terms of the same projection of the angular momentum on the internuclear axis.) For a given R and L, the classical energy E takes only several *discrete* values. However, as L varies over a *continuous* set of values, so does the classical energy E (as it should be in classical physics).

3.3. Crossings of the Energy Terms

Several properties of these energy terms have been studied. We note that in case of small or moderate λ, we observe four terms, both pairs of which have a V-type crossing. As an example, we shall take the plot of the terms for $\lambda = 0.2$ and number the lowest term 1 and the highest term 2; the remaining terms will be numbered 3 and 4, from the lower one to the higher one. Therefore, terms 1 and 2 and terms 3 and 4 undergo V-type crossings, to which we shall refer as $V12$ and $V34$. Using a small-λ approximation by choosing (3.13) as the $p(w)$ solution for the parametric energy terms (essentially, a zero-λ approximation), we can substitute (3.13) into (3.9), which will give it the form below.

$$r = \frac{(1-2w)^{3/2}\sqrt{b^{2/3} - \left(\frac{w}{1-w}\right)^{2/3}}}{w^3\left(b^{2/3} - \left(\frac{1-w}{w}\right)^{4/3}\right)^2} \tag{3.14}$$

For a given b, the terms 3 and 4 are produced by varying w between 0 and w_1. The $V34$ crossing occurs at the value of w where $r(w)$ has a minimum [1.19]. Therefore, setting the derivative dr/dw to zero, we obtain the equation whose solution for w in the range $0 < w < w_1$ gives us the point on the parametric axis which produces the $V34$ crossing.

$$9w^{4/3}(1-w)^{4/3}(w^{4/3} + b^{4/3}(1-w)^{4/3}) = b^{2/3}(1 - 4w + 22w^2 - 36w^3 + 18w^4) \tag{3.15}$$

This equation has no dependence on λ and is therefore equivalent to the Coulomb-potential case described in Section 1. Therefore, an analytical solution exists for (3.15), which is shown in (1.13). Going back to the w-parametrization, we obtain the analytical solution of (3.15):

$$w_{V34} = \frac{1}{1 + \left(b^{1/3} + \frac{(b-1)^{1/3}}{b^{1/6}}\left(\left(\sqrt{b}+1\right)^{1/3} + \left(\sqrt{b}-1\right)^{1/3}\right)\right)^{3/2}} \tag{3.16}$$

Substituting it into (3.9) and using the numerical solution for p of (3.10), we obtain the semi-analytical dependence $r_{V34}(\lambda)$ for a given b. Below is the plot for $b = 3$.

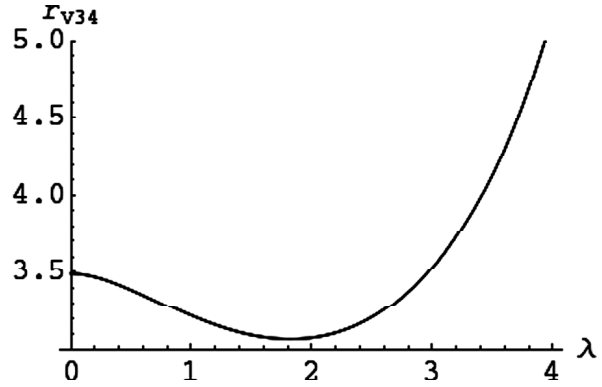

Figure 3.11: Semi-analytical plot of $r_{V34}(\lambda)$ for $b = 3$

Since the plot in Fig. 3.11 was obtained using a zero-λ approximation for the point of the *V*34 crossing, we also graphed this dependence numerically point by point. The graph below for the same *b* shows that in relation to terms 3 and 4, this approximation works well even for moderate values of λ.

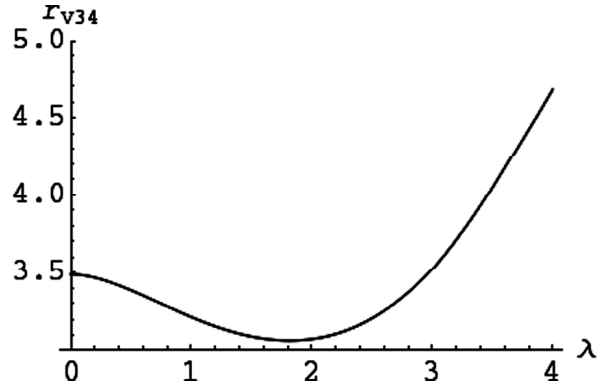

Figure 3.12: Numerical plot of r_{V34} (λ) for b = 3

The energy of the *V*34 crossing can be obtained semi-analytically by substituting the numerical solution for *p* of (3.10) into (3.8), and by further substituting (3.16) into the resulting formula. It could be seen that as λ grows, the energy of the crossing grows and at a relatively large λ becomes positive. A numerical graph can also be made in a fashion similar to Fig. 3.12. A visual comparison shows a good similarity between the two. Below, a numerical graph is given for b = 3.

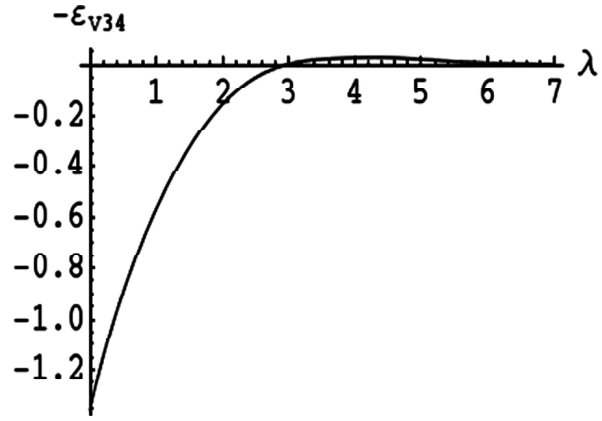

Figure 3.13: Numerical plot of $-\varepsilon_{V34}$(λ) for b = 3

As we see, the energy of the *V*34 crossing becomes positive after λ = 2.96, has a maximum, and later asymptotically approaches zero. For b = 4/3, the *V*34 crossing reaches zero energy at λ = 2.13.

The shape of the terms 3 and 4 is also affected by the screening. Term 3, whose energy increases as *r* increases, becomes nearly horizontal at energy – 0.5 at a certain value of λ; at further λ, its energy decreases with *r*. For b = 3, this value of λ is about 1.1; for b = 4/3, it is about 0.7. The plots are shown below.

For V_{12} crossing, the small-λ approximation is not applicable since this crossing is not observed at λ = 0. Therefore, only numerical methods were used. A situation of particular interest is the behavior of term 1 at very small *r*, because as $r \to 0$ it corresponds to the energy of the hydrogenic ion of the nuclear charge $Z + Z'$ [1.25]. The point with the smallest *r* is the V_{12} crossing. A comparison was made of the dependence of the electronic energy on the screening parameter λ between [1.25] and the limiting case $r \to 0$ in our situation. Since in the paper mentioned

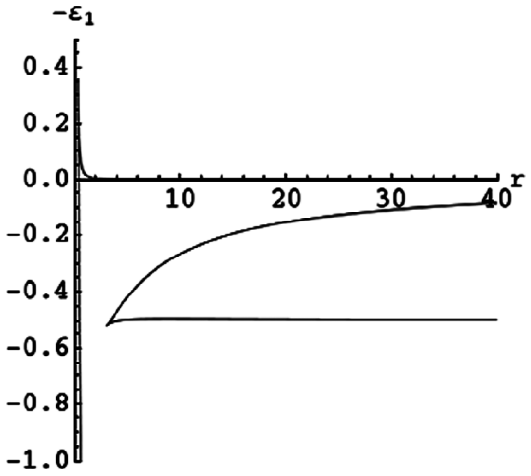

Figure 3.14: Classical energy terms for $b = 3$ at $\lambda = 1.1$; term 3 is nearly constant at energy $-\varepsilon_1 = -0.5$

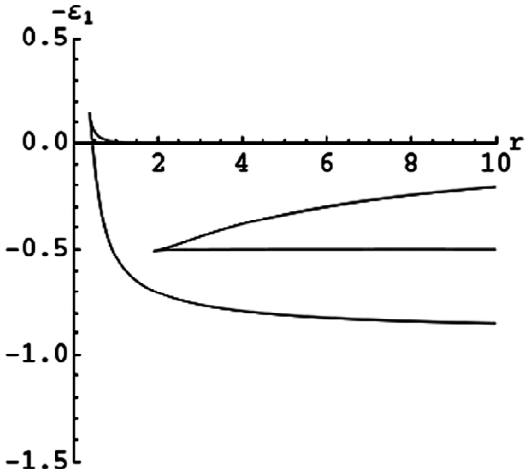

Figure 3.15: The same as Fig. 3.14 for $b = 4/3$ at $\lambda = 0.7$

above, the calculation was performed for a single Coulomb center Z, we had to re-scale the quantities to make a valid comparison. The electronic energies are related as $\varepsilon_1^{(TCC)} = (1 + b)^2 \varepsilon_1^{(OCC)}$, where OCC stands for "one Coulomb center". Since the scaling for the screening parameter in the OCC case did not include R (the internuclear distance), the scaling factor between the screening parameter includes r: $\lambda^{(TCC)} = r(1 + b)\lambda^{(OCC)}$. Taking this into account, we can plot the energy dependence on λ for the limiting case $r \to 0$.

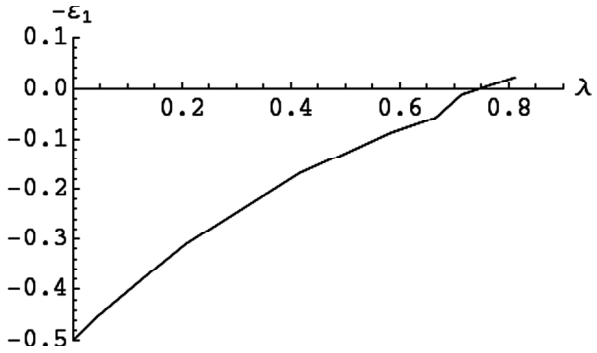

Figure 3.16: Plot of the energy of the electron versus the scaled screening factor for $b = 3$ in the limit $r \to 0$

Below is the dependence obtained in [1.25] for OCC:

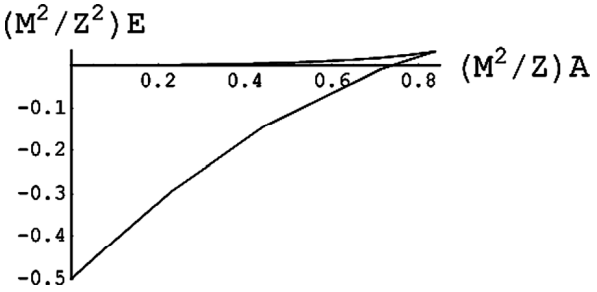

Figure 3.17: Plot of the energy of the electron in a OCC system versus the scaled screening factor

3.4. The Effect of the Plasma Screening on the Internuclear Potential

Another aspect of this problem worth studying is the internuclear potential. Previously its properties were studied for the same system with $\lambda = 0$ and a magnetic field parallel to the internuclear axis [1.20]. Particularly, the magnetic field created a deep minimum in the internuclear potential, which stabilized the nuclear motion and transformed a Rydberg quasi-molecule into a real molecule. Here we shall investigate the effect of the screening on the internuclear potential. Its form in atomic units is

$$U_{\text{int}} = \frac{ZZ'}{R} + E \tag{3.17}$$

where E is the electronic energy. Using the scaled quantities from (3.4), we have the scaled internuclear potential

$$u_{\text{int}} = \frac{bZ}{r} - \varepsilon_1 \tag{3.18}$$

where $U_{\text{int}} = (Z/L)^2 u_{\text{int}}$. By plotting its dependence on r, we found out that in cases of $Z > 1$ the screening tends to flatten the minimum, producing the effect opposite to the one of the magnetic field. Compare the plots of $u_{\text{int}}(r)$ in the case of $Z = 2$, $b = 2$ for $\lambda = 0$ and $\lambda = 0.3$.

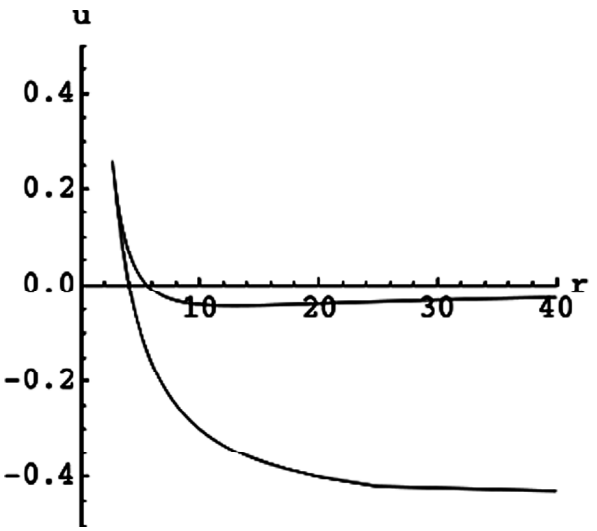

Figure 3.18: The plot of the scaled internuclear potential versus the scaled internuclear distance for $Z = 2$, $Z' = 4$, $\lambda = 0$

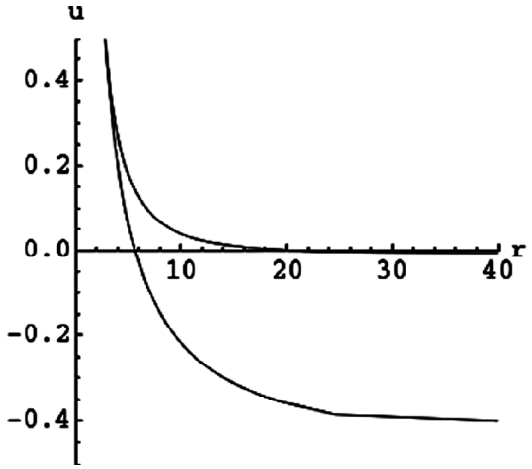

Figure 3.19: The plot of the scaled internuclear potential versus the scaled internuclear distance for $Z = 2$, $Z' = 4$, $\lambda = 0.3$

The screening increases the potential of the point of intersection of the two branches; the upper branch, which has a very shallow minimum at $\lambda = 0$, loses it as λ increases.

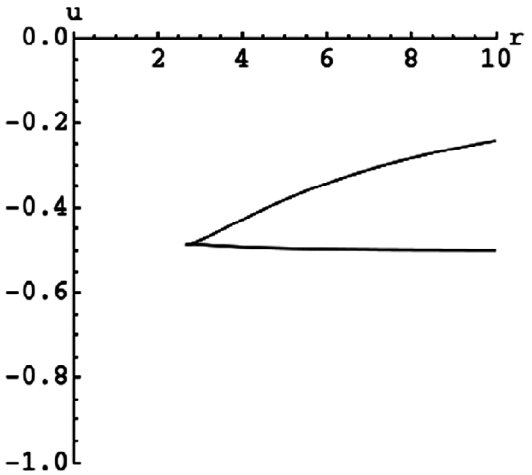

Figure 3.20: The plot of the scaled internuclear potential versus the scaled internuclear distance for $Z = 1$, $Z' = 2$, $\lambda = 0$

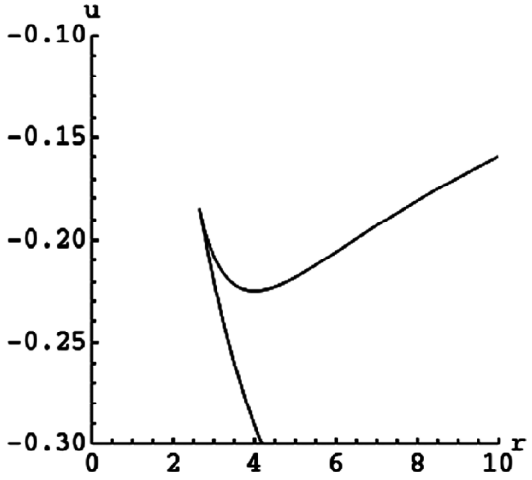

Figure 3.21: The plot of the scaled internuclear potential versus the scaled internuclear distance for $Z = 1$, $Z' = 2$, $\lambda = 0.3$

A completely different behavior was observed for $Z = 1$. A small λ creates a deep minimum in the upper branch of the potential. For comparison, we present the plots of the potential in the case of $Z = 1$, $b = 2$ for $\lambda = 0$ and $\lambda = 0.3$.

The figures above reveal the case of the screening stabilization of the nuclear motion for the case of $Z = 1$ and destabilization for $Z > 1$.

3.5. The Effect of the Plasma Screening on the Continuum Lowering

Our analysis of the stability of the electronic motion shows results similar to those obtained previously in [1.18, 1.19]. Namely, term 3 corresponds to a stable motion while term 4 - to an unstable motion. So, *the crossing point of terms 3 and 4 corresponds to the transition from the stable motion to the unstable motion, leading the electron to the zero energy (i.e., to the free motion) along term 4, which constitutes the ionization of the molecule*.

Therefore, we arrive at the following. For the ionization of the hydrogenlike ion of the nuclear charge Z_{min} perturbed by the charge Z_{max}, it is sufficient to reach the scaled energy $\varepsilon_c(b) = \varepsilon(w_{V34}(b), b) < 0$. At that point, the electron switches to the unstable motion and the radius of its orbit increases without a limit. This constitutes CL by the amount of $Z < 1/R > | \varepsilon(w_{V34}(b), b) |$, where $< 1/R >$ is the value of the inverse distance of the nearest neighbor ion from the radiating ion averaged over the ensemble of perturbing ions.

Thus, obtaining CL in the ionization channel requires calculations of the scaled energy ε at the crossing point w_{V34} of terms 3 and 4.

CL for the "default" ($\lambda = 0$) TCC system was studied in [1.21]. Particularly, the scaled CL energy $\lambda_c(b) = \varepsilon(w_{V34}(b), b) = \Delta E/(Z < 1/R >)$ was graphed on a double-logarithmic scale, where ε is defined in (1.3) and w_{V34} is given by (3.16). The graph is given below; "lg x" stands for "$\log_{10} x$".

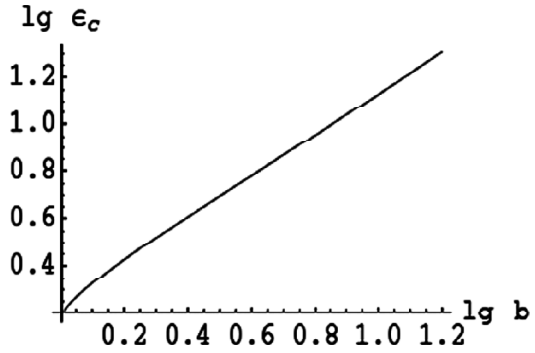

Figure 3.22: The plot of the CL energy versus b on a double logarithmic scale for $\lambda = 0$

We have made several plots of $\varepsilon_c(b)$ for several values of λ. A numerical value for w_{V34} was taken to increase precision.

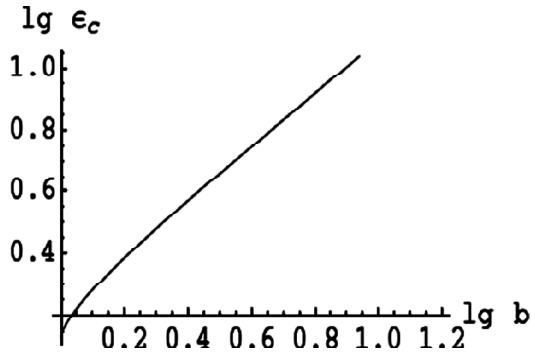

Figure 3.23: The plot of the CL energy versus b on a double logarithmic scale for $\lambda = 0.1$

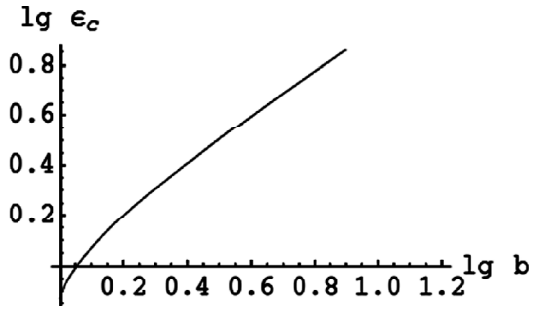

Figure 3.24: The plot of the CL energy versus *b* on a double logarithmic scale for λ = 0.5

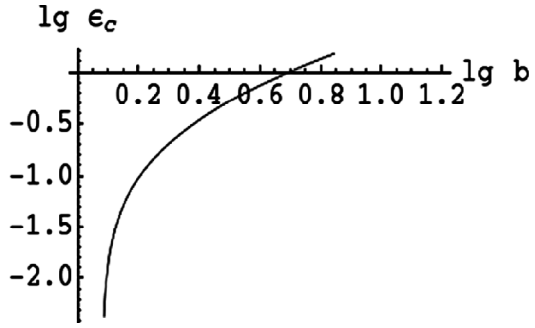

Figure 3.25: The plot of the CL energy versus *b* on a double logarithmic scale for λ = 2

From the figures above we can see that the plasma screening decreases the value of CL in the ionization channel. Also, starting from about $\lambda = 1.7$, we observe the "cutoff " value of $b > 1$, below which ε_c becomes negative, i.e., the electron energy at w_{V34} becomes positive. This means that there is no more CL in this ionization channel – instead, the continuum becomes higher than for the isolated hydrogen-like ion of the nuclear charge *Z*. This effect cannot be observed in the logarithmic graphs above because the cutoff value of energy (zero) corresponds to $\lg \varepsilon_c = -\infty$. Below we made the standard, non-logarithmic plots of $\varepsilon_c(b)$ for selected values of λ at which this effect is observed.

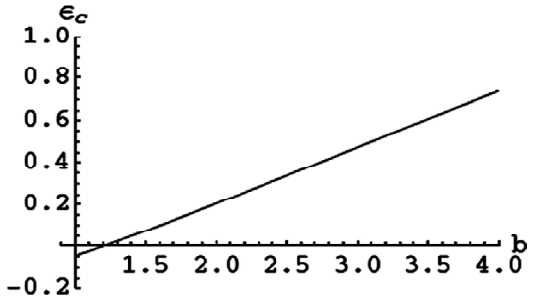

Figure 3.26: The plot of the CL energy versus *b* for λ = 2

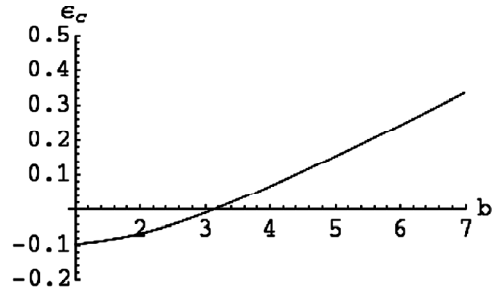

Figure 3.27: The plot of the CL energy versus *b* for λ = 3

In Fig. 3.27 we can see that there is no CL for $b = 2$ and $b = 3$ at $\lambda = 3$.

In Appendices 3B and 3C we present the effects of the electric and magnetic fields on CL. The effect of the magnetic field was observed to decrease the value of CL, similar to the case above, while the electric field increases the value of CL, promoting ionization.

3.6. Conclusions

We studied the effects of the plasma screening on the classical energy terms of the electron in the field of two Coulomb centers. We provided analytical results for the small values of the screening factor and numerical results for the medium values.

We found that the plasma screening leads to the appearance of the fourth energy term – in addition to the three classical energy terms with no screening. This term exhibits a *V*-type crossing with the lowest energy term. The two highest energy terms continue having a *V*-type crossing like at the zero field.

We studied the effect of the screening on the internuclear potential. We found that the nuclear motion was stabilized by screening for $Z = 1$ and destabilized for $Z > 1$.

The effect of the screening on the continuum lowering was studied as well. The plasma screening decreases the value of CL in the ionization channel, similar to the effect of the magnetic field [1.20].

APPENDIX 3A
THE ANALYTICAL EXPRESSION FOR THE LIMIT w_1 IN Eq. (3.11) IN THE SMALL-λ APPROXIMATION

$$-\frac{-b-5\lambda+1}{8\lambda}-\frac{1}{2}\sqrt{\left(\frac{(-b-5\lambda+1)^2}{16\lambda^2}-\frac{4\lambda^2+b\lambda-3\lambda+b-1}{3\lambda^2}+\frac{1}{6\sqrt[3]{2}\lambda^2}((2(4\lambda^2+b\lambda-3\lambda+b-1)^3\right.}$$

$$-144(-\lambda-1)\lambda^2(4\lambda^2+b\lambda-3\lambda+b-1)-9(-5\lambda^2-b\lambda+\lambda)(-\lambda^2+3\lambda+2)(4\lambda^2+b\lambda-3\lambda+b-1)$$

$$+27(-\lambda-1)(-5\lambda^2-b\lambda+\lambda)^2+54\lambda^2(-\lambda^2+3\lambda+2)^2+\sqrt{}((2(4\lambda^2+b\lambda-3\lambda+b-1)^3$$

$$-144(-\lambda-1)\lambda^2(4\lambda^2+b\lambda-3\lambda+b-1)-9(-5\lambda^2-b\lambda+\lambda)(-\lambda^2+3\lambda+2)(4\lambda^2+b\lambda-3\lambda+b-1)$$

$$+27(-\lambda-1)(-5\lambda^2-b\lambda+\lambda)^2+54\lambda^2(-\lambda^2+3\lambda+2)^2)^2-4(\lambda^4+5b\lambda^3-b^2\lambda^2+11b\lambda^2-2\lambda^2+2b^2\lambda$$

$$-2b\lambda+b^2-2b+1)^3))\wedge(1/3))+(\lambda^4+5b\lambda^3+b^2\lambda^2+11b\lambda^2-2\lambda^2+2b^2\lambda-2b\lambda+b^2-2b+1)/$$

$$(32^{2/3}\lambda^2(2(4\lambda^2+b\lambda-3\lambda+b-1)^3-144(-\lambda-1)\lambda^2(4\lambda^2+b\lambda-3\lambda+b-1)$$

$$-9(-5\lambda^2-b\lambda+\lambda)(-\lambda^2+3\lambda+2)(4\lambda^2+b\lambda-3\lambda+b-1)+27(-\lambda-1)(-5\lambda^2-b\lambda+\lambda)^2$$

$$+54\lambda^2(-\lambda^2+3\lambda+2)^2+\sqrt{}((2(4\lambda^2+b\lambda-3\lambda+b-1)^3-144(-\lambda-1)\lambda^2(4\lambda^2+b\lambda-3\lambda+b-1)$$

$$-9(-5\lambda^2-b\lambda+\lambda)(-\lambda^2+3\lambda+2)(4\lambda^2+b\lambda-3\lambda+b-1)+27(-\lambda-1)(-5\lambda^2-b\lambda+\lambda)^2$$

$$\left.+54\lambda^2(-\lambda^2+3\lambda+2)^2)^2-4(\lambda^2+5b\lambda^3+b^2\lambda^2+11b\lambda^2-2\lambda^2+2b^2\lambda-2b\lambda+b^2-2b+1^3))\wedge(1/3))\right)$$

$$+\frac{1}{2}\sqrt{\left(\frac{(-b-5\lambda+1)^2}{8\lambda^2}-\frac{2(4\lambda^2+b\lambda-3\lambda+b-1)}{3\lambda^2}-\frac{1}{6\sqrt[3]{2}\lambda^2}((2(4\lambda^2+b\lambda-3\lambda+b-1)^3\right.}$$

$$-144(-\lambda-1)\lambda^2(4\lambda^2+b\lambda-3\lambda+b-1)-9(-5\lambda^2-b\lambda+\lambda)(-\lambda^2+3\lambda+2)(4\lambda^2+b\lambda-3\lambda+b-1)$$

$$+27(-\lambda-1)(-5\lambda^2-b\lambda+\lambda)^2+54\lambda^2(-\lambda^2+3\lambda+2)^2+\sqrt{((2(4\lambda^2+b\lambda-3\lambda+b-1)^3}$$

$$-144(-\lambda-1)\lambda^2(4\lambda^2+b\lambda-3\lambda+b-1)-9(-5\lambda^2-b\lambda+\lambda)(-\lambda^2+3\lambda+2)(4\lambda^2+b\lambda-3\lambda+b-1)$$

$$+27(-\lambda-1)(-5\lambda^2-b\lambda+\lambda)^2+54\lambda^2(-\lambda^2+3\lambda+2)^2)^2-4(\lambda^4+5b\lambda^3-b^2\lambda^2+11b\lambda^2-2\lambda^2+2b^2\lambda$$

$$-2b\lambda+b^2-2b+1)^3))\wedge(1/3))-(\lambda^4+5b\lambda^3+b^2\lambda^2+11b\lambda^2-2\lambda^2+2b^2\lambda-2b\lambda+b^2-2b+1)/$$

$$(32^{2/3}\lambda^2(2(4\lambda^2+b\lambda-3\lambda+b-1)^3-144(-\lambda-1)\lambda^2(4\lambda^2+b\lambda-3\lambda+b-1)$$

$$-9(-5\lambda^2-b\lambda+\lambda)(-\lambda^2+3\lambda+2)(4\lambda^2+b\lambda-3\lambda+b-1)+27(-\lambda-1)(-5\lambda^2-b\lambda+\lambda)^2$$

$$+54\lambda^2(-\lambda^2+3\lambda+2)^2+\sqrt{((2(4\lambda^2+b\lambda-3\lambda+b-1)^3-144(-\lambda-1)\lambda^2(4\lambda^2+b\lambda-3\lambda+b-1)}$$

$$-9(-5\lambda^2-b\lambda+\lambda)(-\lambda^2+3\lambda+2)(4\lambda^2+b\lambda-3\lambda+b-1)+27(-\lambda-1)(-5\lambda^2-b\lambda+\lambda)^2$$

$$+54\lambda^2(-\lambda^2+3\lambda+2)^2)^2-4(\lambda^2+5b\lambda^3+b^2\lambda^2+11b\lambda^2-2\lambda^2+2b^2\lambda-2b\lambda+b^2-2b+1)^3))\wedge(1/3))$$

$$\left.\left.\left.\left.\left.-\frac{(-b-5\lambda+1)^3}{8\lambda^3}+\frac{(4\lambda^2+b\lambda-3\lambda+b-1)(-b-5\lambda+1)}{\lambda^3}-\frac{4(-\lambda^2+3\lambda+2)}{\lambda^2}\right)\right/\right.\right.\right.$$

$$\left.\left.\left.\left.\left.4\sqrt{\left(\frac{(-b-5\lambda+1)^2}{16\lambda^2}-\frac{4\lambda^2+b\lambda-3\lambda+b-1}{3\lambda^2}+\frac{1}{6\sqrt[3]{2}\lambda^2}((2(4\lambda^2+b\lambda-3\lambda+b-1)^3\right.}\right.\right.\right.\right.$$

$$-144(-\lambda-1)\lambda^2(4\lambda^2+b\lambda-3\lambda+b-1)-9(-5\lambda^2-b\lambda+\lambda)(-\lambda^2+3\lambda+2)(4\lambda^2+b\lambda-3\lambda+b-1)$$

$$+27(-\lambda-1)(-5\lambda^2-b\lambda+\lambda)^2+54\lambda^2(-\lambda^2+3\lambda+2)^2+\sqrt{((2(4\lambda^2+b\lambda-3\lambda+b-1)^3}$$

$$-144(-\lambda-1)\lambda^2(4\lambda^2+b\lambda-3\lambda+b-1)-9(-5\lambda^2-b\lambda+\lambda)(-\lambda^2+3\lambda+2)(4\lambda^2+b\lambda-3\lambda+b-1)$$

$$+27(-\lambda-1)(-5\lambda^2-b\lambda+\lambda)^2+54\lambda^2(-\lambda^2+3\lambda+2)^2)^2-4(\lambda^4+5b\lambda^3-b^2\lambda^2+11b\lambda^2-2\lambda^2+2b^2\lambda$$

$$-2b\lambda+b^2-2b+1)^3))\wedge(1/3))+(\lambda^4+5b\lambda^3+b^2\lambda^2+11b\lambda^2-2\lambda^2+2b^2\lambda-2b\lambda+b^2-2b+1)/$$

$$(32^{2/3}\lambda^2(2(4\lambda^2+b\lambda-3\lambda+b-1)^3-144(-\lambda-1)\lambda^2(4\lambda^2+b\lambda-3\lambda+b-1)$$

$$-9(-5\lambda^2-b\lambda+\lambda)(-\lambda^2+3\lambda+2)(4\lambda^2+b\lambda-3\lambda+b-1)+27(-\lambda-1)(-5\lambda^2-b\lambda+\lambda)^2$$

$$+54\lambda^2(-\lambda^2+3\lambda+2)^2+\sqrt{((2(4\lambda^2+b\lambda-3\lambda+b-1)^3-144(-\lambda-1)\lambda^2(4\lambda^2+b\lambda-3\lambda+b-1)}$$

$$-9(-5\lambda^2-b\lambda+\lambda)(-\lambda^2+3\lambda+2)(4\lambda^2+b\lambda-3\lambda+b-1)+27(-\lambda-1)(-5\lambda^2-b\lambda+\lambda)^2$$

$$\left.\left.\left.\left.+54\lambda^2(-\lambda^2+3\lambda+2)^2)^2-4(\lambda^2+5b\lambda^3+b^2\lambda^2+11b\lambda^2-2\lambda^2+2b^2\lambda-2b\lambda+b^2-2b+1^3))\wedge(1/3))\right)\right)\right)\right)$$

APPENDIX 3B
THE EFFECT OF THE ELECTRIC FIELD ON CONTINUUM LOWERING

Using the value of the scaled energy of the electron in the TCC system given in (2.5) with the substitution of the numeric or approximate solution for p from (2.10) into (2.5) and (2.7) and the further substitution of ℓ from (2.7) into (2.5), we obtain the dependence of the scaled energy on the scaled coordinate w in the situation considered in Section 2, where the electric field was parallel to the internuclear axis. Then we numerically find the point on the w-axis corresponding to the $V34$ crossing for a given value of the scaled electric field f and substitute it into the formula for the scaled energy, obtaining the critical energy, which is the value of CL.

Below are a few logarithmic plots (lg ε_c versus lg b) made for selected values of f.

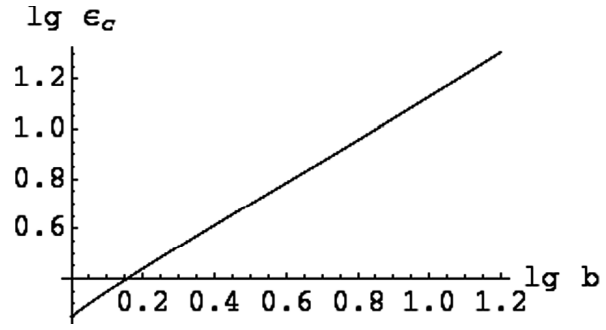

Figure 3.B1: The plot of the CL energy versus b for f = 0.1

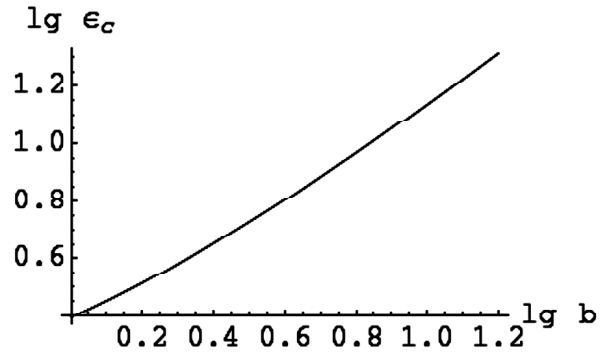

Figure 3.B2: The plot of the CL energy versus b for f = 1

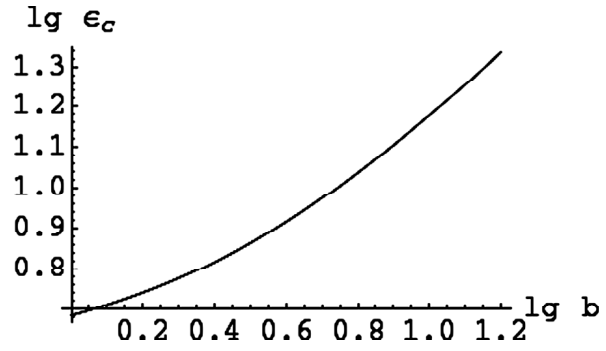

Figure 3.B3: The plot of the CL energy versus b for f = 10

CL increases as the electric field increases. This is expected because the electric field promotes ionization.

APPENDIX 3C
THE EFFECT OF THE MAGNETIC FIELD ON CONTINUUM LOWERING

In the case of the magnetic field **B** parallel to the internuclear axis, the default energy given in (1.2) will acquire an additional term

$$\Omega L + \frac{\Omega^2 \rho^2}{2} \tag{3.C.1}$$

where $\Omega = B/(2c)$ is the Larmor frequency. We apply the same method as we used in the beginning of each chapter to find the energy dependent on one spatial parameter. Substituting the scaled quantities as defined in (3.4) and defining $\omega = \Omega L^3/Z^2$, taking the derivatives by w and p and setting them equal to zero, solving for p and ℓ, substituting them back into the formula for energy, and further substituting the parameter γ as given in (1.10), we arrive at the following expressions of the scaled energy $\varepsilon = -ER/Z$: and the scaled internuclear distance r:

$$\varepsilon = \frac{(\gamma^4 - 2\gamma + b^{2/3}(2\gamma^3 - 1))\sqrt{(\gamma^3+1)(b^{2/3}\gamma^2 - 1)}}{2\gamma(\gamma^3-1)^{3/2}} + \frac{\gamma^2(b^{2/3} - \gamma^4)}{(\gamma^3+1)^2(b^{2/3}\gamma^2 - 1)}\omega\left(\omega + \sqrt{\omega^2 + \frac{(\gamma^3+1)^{5/2}(b^{2/3}\gamma^2-1)^{3/2}}{\gamma^3(\gamma^3-1)^{3/2}}}\right) \tag{3.C.2}$$

$$r = \frac{(\gamma^3+1)^4(b^{2/3}\gamma^2-1)^2}{\gamma^4(b^{2/3}-\gamma^4)^2\left(\omega^2 + \frac{(\gamma^3+1)^{5/2}(b^{2/3}\gamma^2-1)^{3/2}}{\gamma^3(\gamma^3-1)^{3/2}}\right)} \tag{3.C.3}$$

To find the point of the $V34$ crossing, we take the derivative of r by γ and set it equal to zero. The numerical solution for this equation determines the value of γ corresponding to the minimum of $r(\gamma)$ for given b and ω, which corresponds to the crossing. Substituting it to the expression for the energy in (3.C.2), we obtain $\varepsilon_c(b, \omega)$ – the dependence of CL on b for a given ω.

Below we present several double-logarithmic plots, similar to those in Section 3.5 and Appendix 3B, for selected values of ω.

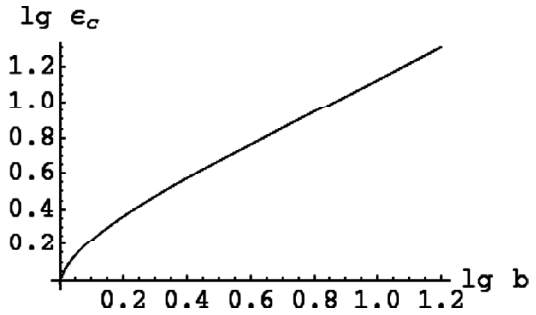

Figure 3.C1: The plot of the CL energy versus b on a double-logarithmic scale for $\omega = 0.5$

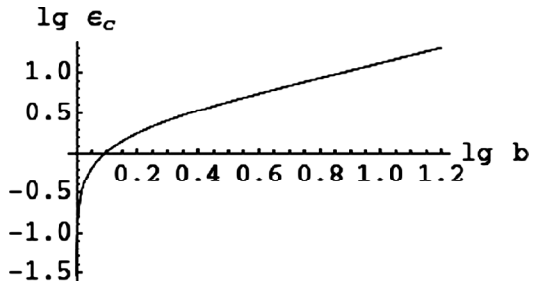

Figure 3.C2: The plot of the CL energy versus b on a double-logarithmic scale for $\omega = 1$

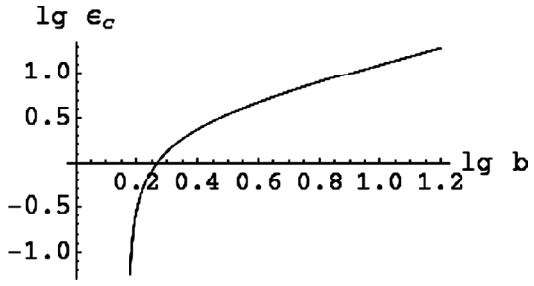

Figure 3.C3: The plot of the CL energy versus b on a double-logarithmic scale for ω = 2

From the graphs in Figs. 3.C1 – 3.C3 it is seen that the effect of the magnetic field on CL is similar to the effect of the plasma screening – it decreases CL. The "cutoff " values of *b*, below which there is no CL for a given ω, are also observed as ω becomes large. For example, for ω = 2.8 CL at *b* = 2 vanishes, so the values of *b* corresponding to CL start at *b* > 2. At ω = 4.3, CL starts at *b* > 3. (See Figs. 3.C4 and 3.C5 below.)

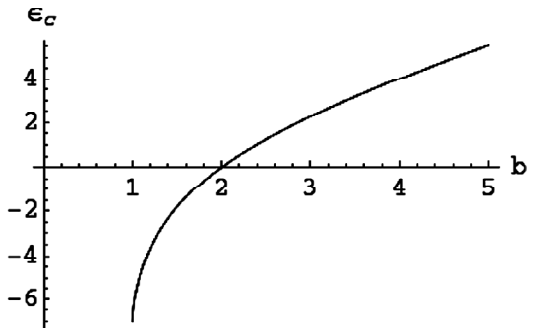

Figure 3.C4: The plot of the CL energy versus *b* for ω = 2.8

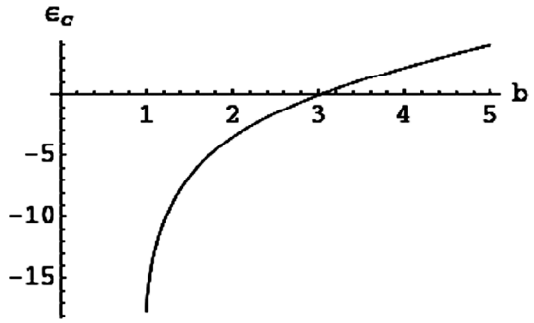

Figure 3.C5: The plot of the CL energy versus *b* for ω = 4.3

4. HELICAL AND CIRCULAR STATES OF DIATOMIC RYDBERG QUASIMOLECULES IN A LASER FIELD

4.1. Introduction

In the previous works [1.18-1.20, 1.24, 1.25, 1.28, 1.34] and the previous chapters, analytical studies of circular Rydberg states of two-Coulomb-center systems consisting of two nuclei of charges *Z* and *Z*′, separated by a distance *R*, and one electron were carried out. Energy terms of these Rydberg quasimolecules for a field-free case [1.18, 1.19] were obtained, as well as under a static electric field ([1.24] and Section 2) or under a static magnetic field [1.20], and crossings of the energy terms were studied – the crossings that enhance charge exchange in these systems.

The analysis was not confined to circular orbits of the electron. For example, paper [1.19] studied in detail *helical* Rydberg states of these Rydberg quasimolecules. In order to make those results more transparent, we briefly outline here the scheme of that analysis. In cylindrical coordinates (z, ρ, φ) with the z-axis along the internuclear axis, using the axial symmetry of the problem, the z- and ρ-motions can be separated from the φ-motion. The φ-motion can be then determined from the calculated ρ-motion. Equilibrium points of the two-dimensional motion in the $z\rho$-space were studied and a condition distinguishing between two physically different cases, where the effective potential energy either has a two-dimensional minimum in the $z\rho$-space or has a saddle point in the $z\rho$-space, was explicitly derived. In particular, it turned out that the boundary between these two cases corresponds to the point of crossing of the upper and middle energy terms (out of the three energy terms in this system). For the stable motion, the trajectory was found to be a helix on the surface of a cone, with axis coinciding with the internuclear axis. In this *helical* state, the electron, while spiraling on the surface of the cone, oscillates between two end-circles which result from cutting the cone by two parallel planes perpendicular to its axis (Fig. 1.1).

In the present chapter we study such Rydberg quasimolecules under a laser field. For the situation where the laser field is linearly-polarized along the internuclear axis, we found an analytical solution for the stable helical motion of the electron valid for wide ranges of the laser field strength and frequency. We also found resonances, corresponding to a laser-induced unstable motion of the electron, that result in the destruction of the helical states. For the situation where such Rydberg quasimolecules are under a circularly-polarized field, polarization plane being perpendicular to the internuclear axis, we found an analytical solution for circular Rydberg states valid for wide ranges of the laser field strength and frequency. We showed that both under the linearly-polarized laser field and under the circularly-polarized laser field, in the electron radiation spectrum in the addition to the primary spectral component at (or near) the unperturbed revolution frequency of the electron, there appear satellites. We found that for the case of the linearly-polarized laser field, the intensities of the satellites are proportional to the squares of the Bessel functions $J_q^2(s)$, (q = 1, 2, 3, …), where s is proportional to the laser field strength. As for the case of the circularly-polarized field, we demonstrated that there is a red shift of the primary spectral component – the shift linearly proportional to the laser field strength.

4.2. Analytical Solution for the Case of a Linearly-Polarized Laser Field

We consider the case where the laser is polarized parallel to the internuclear axis and oscillates sinusoidally with the frequency ω. The angular momentum L is conserved here due to φ-symmetry. The corresponding Hamiltonian is

$$H = \frac{p_\rho^2 + p_\varphi^2}{2} + \frac{L^2}{2\rho^2} - \frac{Z}{\sqrt{\rho^2 + z^2}} - \frac{Z'}{\sqrt{\rho^2 + (R-z)^2}} + zF\cos\omega t \tag{4.1}$$

Below we scale all frequencies using the factor $(R^3/Z)^{1/2}$: for example, the scaled laser frequency is $\mu = \omega(R^3/Z)^{1/2}$. We also use scaled coordinates as in papers [1.18, 1.19] and the other chapters

$$w = \frac{z}{R}, \qquad v = \frac{\rho}{R} \tag{4.2}$$

where R is the internuclear distance. The origin is at the location of charge Z.

Without the electric field, in the vicinity of the equilibrium the motion in $z\rho$-space corresponds to a two-dimensional harmonic oscillator [1.19]. Its scaled eigen-frequencies are

$$\omega_\pm = \frac{1}{(w^2+v^2)^{3/4}}\sqrt{\frac{1}{1-w} \pm \frac{3w}{\sqrt{(w^2+v^2)((1-w)^2+v^2)}}} \tag{4.3}$$

where the equilibrium value of v connected to w as follows – as in (1.5) and in [1.18, 1.19]:

$$v(w,b)=\sqrt{\frac{w^{2/3}(1-w)^{4/3}-b^{2/3}w^2}{b^{2/3}-w^{2/3}(1-w)^{-2/3}}} \tag{4.4}$$

The motion occurs on the axes (w', v'), which are the original axes (w, v) rotated by an angle α given in [1.19]. The dependence of the angle α on the scaled coordinate w can be expressed in the most compact form by introducing the notation as in (1.15):

$$\gamma=\left(\frac{1}{w}-1\right)^{1/3} \tag{4.5}$$

In the γ-representation it has the form

$$\alpha=\frac{1}{2}\,\mathrm{arctg}\,\frac{\sqrt{(b^{2/3}\gamma^2-1)(\gamma^4-b^{2/3})}}{\gamma(b^{2/3}+\gamma)} \tag{4.6}$$

The scaled eigen-frequencies ω_- and ω_+ are the scaled frequencies of small oscillations about the equilibrium along the coordinates w', v' accordingly.

As we introduce the oscillating electric field, these oscillations become forced, with the forces $F\cos\alpha\cos\omega t$ on w' and $F\sin\alpha\cos\omega t$ on v'. Therefore, the deviations from equilibrium on (w', v') are (see, e.g., textbooks [4.1, 4.2])

$$\delta w'=\frac{f\cos\alpha}{\omega_-^2-\mu^2}\cos\mu\tau,\qquad \delta v'=\frac{f\sin\alpha}{\omega_+^2-\mu^2}\cos\mu\tau \tag{4.7}$$

where $\mu=\omega(R^3/Z)^{1/2}$ and $\tau=t(Z/R^3)^{1/2}$. Now we revert to the original coordinates (w, v) and obtain the equations of motion in the linearly-polarized oscillatory electric field in the vicinity of the equilibrium: the electron follows the circular path corresponding to the case with no electric field with deviations from equilibrium depending on the scaled time τ:

$$\begin{aligned}\delta w&=f\left(\frac{f\cos^2\alpha}{\omega_-^2-\mu^2}+\frac{f\sin^2\alpha}{\omega_+^2-\mu^2}\right)\cos\mu\tau,\\ \delta v&=f\sin\alpha\cos\alpha\left(\frac{1}{\omega_-^2-\mu^2}-\frac{1}{\omega_+^2-\mu^2}\right)\cos\mu\tau\end{aligned} \tag{4.8}$$

From (4.8) it is seen that the strength and frequency of the laser field affect the amplitudes of the forced oscillations on w- and v-axes; in fact, these amplitudes are proportional to the field strength f. The frequencies of the forced oscillations on the axes are equal to that of the laser field, instead of ω_- and ω_+.

Since the Hamiltonian from (4.1) does not depend on φ, the corresponding momentum is conserved:

$$p_\varphi=\rho^2\frac{d\varphi}{dt}\equiv L=\mathrm{const} \tag{4.9}$$

We can re-write (4.9) in the scaled notation as

$$\frac{d\varphi}{d\tau}=\frac{\ell}{v^2(\tau)} \tag{4.10}$$

where $\ell = L/(ZR)^{1/2}$ is the scaled angular momentum. Substituting in (4.10) $\nu(\tau) = \nu_0 + \delta\nu(\tau)$, where $\nu_0(w)$ is the equilibrium value of the scaled radius ν of the electron orbit from (4.4) and $\delta\nu(\tau)$ is given by (4.8), we obtain

$$\frac{d\varphi}{dt} \approx \frac{\ell}{\nu_0^2} - \frac{2\ell}{\nu_0^3}\,\delta\nu(\tau) \tag{4.11}$$

which after the integration with respect to time yields:

$$\varphi(t) \approx \frac{\ell}{\nu_0^2}\,\tau - \frac{2\ell}{\mu\nu_0^3}\, f \sin\alpha\cos\alpha\left(\frac{1}{\omega_-^2 - \mu^2} - \frac{1}{\omega_+^2 - \mu^2}\right)\sin\mu\tau \tag{4.12}$$

From (4.12) it is seen that the φ-motion is a rotation about the internuclear axis with the scaled frequency ℓ/ν_0^2, slightly modulated by oscillations of the scaled radius of the orbit ν at the laser frequency μ (i.e., at the laser frequency ω in the usual notation).

Thus, from (4.8) and (4.12) it is clear that the electron is bound to a conical surface which incorporates the original circular orbit. In Fig. 4.1 below the three-dimensional actual trajectory is plotted for $b = 3$, $f = 1$, $\mu = 1$ at $w = 0.2$.

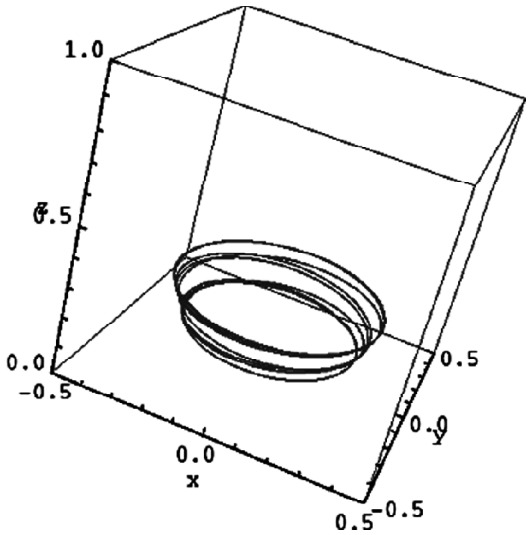

Figure 4.1: The actual trajectory of the electron in the linearly-polarized laser field for $b = 3$, $f = 1$, $\mu = 1$ at $w = 0.2$. The z-axis is along the internuclear axis

The expression for $\varphi(\tau)$ from (4.12), i.e., $\varphi(t\,(Z/R^3)^{1/2})$, enters the following Fourier-transform that determines the amplitude of the power spectrum of the electron radiation

$$A_l(\Delta) = \frac{1}{2}\int_0^\infty dt \cos\left(\Delta t - \varphi\left(t\sqrt{\frac{Z}{R^3}}\right)\right) \tag{4.13}$$

where Δ is the radiation frequency measured, e.g., by a spectrometer. The sinusoidal modulation of the phase φ is analogous to the situation where hydrogen spectral lines are modified by an external monochromatic field at the frequency ω, the latter problem being solved analytically by Blochinzew as early as in 1933 [4.3] (a further study can be found, e.g., in book [4.4]).

From Blochinzew's results it follows for our case in the electron radiation spectrum, this helical motion should manifest as follows. The most intense emission would be at the frequency $\Omega = d\varphi/dt$ of the rapid φ-motion. In

addition, there will be satellites at the frequencies $\Omega \pm q\omega$, where q = 1, 2, 3, …, whose relative intensities I_q are controlled by the Bessel functions $J_q(s)$:

$$I_q = J_q^2(s), \quad s = \frac{2\ell}{\mu\nu_0^3} f \sin\alpha \cos\alpha \left(\frac{1}{\omega_-^2 - \mu^2} - \frac{1}{\omega_+^2 - \mu^2} \right) \tag{4.14}$$

The oscillatory motion of the electron in the $z\rho$-space with the laser frequency ω should lead also to the radiation at this frequency. However, since $\omega << \Omega$, this spectral component would be far away from the primary spectral line and its satellites.

From (4.8) it is also seen that there are resonances when the laser frequency is equal to one of the eigen-frequencies of the motion in the $z\rho$-space, i.e., when either $\mu = \omega_+$ or $\mu = \omega_-$. It turns out that these conditions yield three resonance points on the w-axis for the laser field frequency μ below a certain critical value μ_c, or five resonance points for $\mu > \mu_c$ – see the figures below.

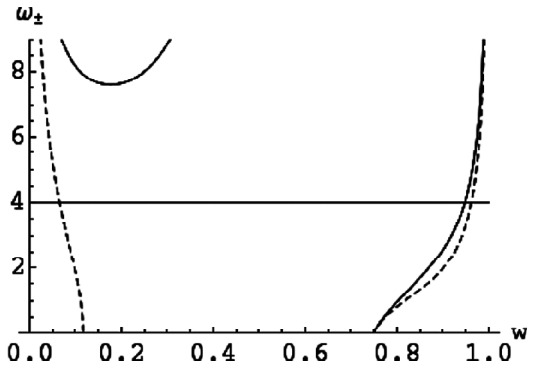

Figure 4.2: Eigen-frequencies of the motion in the $z\rho$-space ω_+ (solid curves) and ω_- (dashed curves) versus w, i.e., versus the scaled z-coordinate of original circular Rydberg state. The scaled laser frequency μ is shown by the horizontal straight line. The plot is for b = 3 and μ = 4. Three resonant points are seen

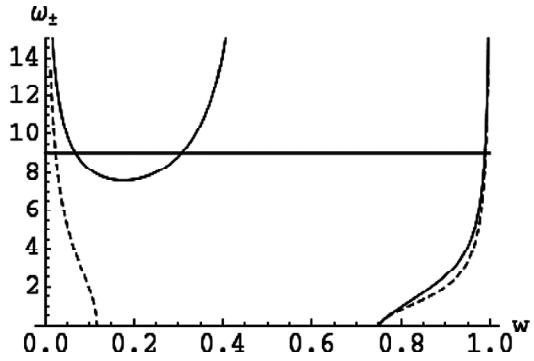

Figure 4.3: Same as in Fig. 4.2, but for b = 3 and μ = 9. Five resonant points are seen

For instance, in the case of b = 3, for μ = 8, we observe resonances at the following five values of w: 0.02883, 0.1106, 0.2497, 0.9852, 0.9878. The critical value corresponds to the minimum of $\omega_+(w)$ for a given b in the interval $0 < w < w_1$ at the equilibrium point (the equilibrium scaled coordinate v being expressed via w by (4.4)). Calculating the derivative of ω_+ with respect to w and setting it equal to zero, we find the point of the minimum. The value of ω_+ at this point will be equal to the critical value of the scaled laser frequency μ_c. For example, for b = 3 at w = 0.17642 (the minimum of ω_+ in Figs. 4.2 and 4.3) this critical value is μ_c = 7.5944. As the ratio of nuclear charges b increases, so does also the critical value μ_c of the scaled laser frequency.

These resonances correspond to a laser-induced unstable motion of the electron that result in the destruction of the helical states. This is illustrated in Fig. 4.4 showing the three-dimensional actual trajectory of the electron (for various directions of its initial velocity) for a resonance case where $b = 3$, $f = 1$, $\mu = 8$, and $w = 0.111$ ($w = 0.111$ is one of the three values of w, at which the laser frequency μ coincides with the eigen-frequency ω_+). A striking difference is seen compared to the stable helical motion depicted in Fig. 4.1: the resonance destroyed the helical state.

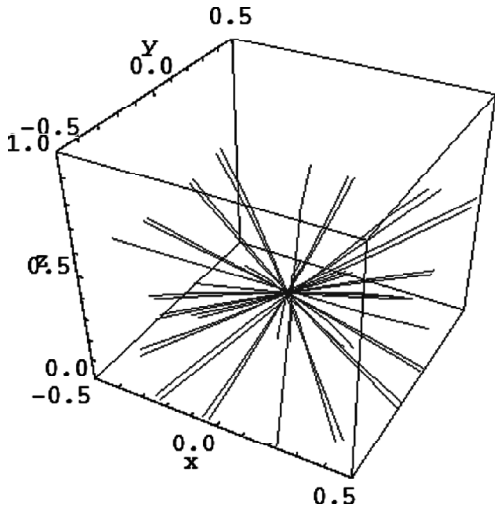

Figure 4.4: The actual trajectory of the electron (for various directions of its initial velocity) in the linearly-polarized laser field for a resonance case where $b = 3$, $f = 1$, $\mu = 8$, and $w = 0.111$. The z-axis is along the internuclear axis

4.3. Analytical Solution for the Case of a Circularly-Polarized Laser Field

Now we consider the case of a circular polarization of the laser field, polarization plane being perpendicular to the internuclear axis. The laser field varies as

$$\mathbf{F} = F(\mathbf{e}_x \cos \omega t + \mathbf{e}_y \sin \omega t) \tag{4.15}$$

where $\mathbf{e}_x$ and $\mathbf{e}_y$ are the unit vectors along the x- and y-axes, F is the amplitude and ω is the frequency. The Hamiltonian for the electron in this configuration will take the following form.

$$H = \frac{1}{2}\left(p_\rho^2 + p_z^2 + \frac{p_\varphi^2}{\rho} \right) - \frac{Z}{\sqrt{\rho^2 + z^2}} - \frac{Z'}{\sqrt{\rho^2 + (R-z)^2}} + F\rho \cos(\varphi - \varphi_0) \tag{4.16}$$

where we introduced $\varphi_0 = \omega t$. As in [1.19], we consider φ-motion to be the rapid subsystem, i.e. $d\varphi/dt$ is much greater than the laser frequency ω and the frequencies of z- and ρ-motion. The canonical equations for the φ-motion obtained from (4.16) are

$$\frac{d\varphi}{dt} = \frac{\partial H}{\partial p_\varphi} = \frac{p_\varphi}{\rho^2} \tag{4.17}$$

$$\frac{dp_\varphi}{dt} = -\frac{\partial H}{\partial \varphi} = F\rho \sin(\varphi - \varphi_0) \tag{4.18}$$

Combining (4.17) and (4.18), we get

$$\frac{d^2\varphi}{dt^2} = \frac{F}{\rho} \sin(\varphi - \varphi_0) \tag{4.19}$$

After a substitution $\varphi - \varphi_0 = \theta + \pi$, (4.19) becomes

$$\frac{d^2\theta}{dt^2} = -\frac{F}{\rho}\sin\theta \tag{4.20}$$

which is the equation of motion of a mathematical pendulum of length ρ in gravity F. Its two possible modes are libration and rotation; since θ is the rapid coordinate, we have the case of rotation. The solution for $\theta(t)$ is well-known and can be expressed in terms of Jacobi amplitude:

$$\theta(t) = 2\,\mathrm{am}\left(\frac{\Omega t}{2}, \frac{4F}{\rho\Omega^2}\right) \tag{4.21}$$

Here we denoted $d\theta/dt$ at $t = 0$ as Ω. For rapid rotations, the change in the angular speed on θ is insignificant compared to the initial speed and $d\theta/dt \approx \Omega$.

The expression for $\theta(t)$ enters the following Fourier-transform that determines the amplitude of the power spectrum of the electron radiation:

$$A_c\left(\Delta, \frac{4F}{\rho\Omega^2}\right) = \frac{1}{\pi}\int_0^\infty dt\cos\left(\Delta t - \theta\left(t, \frac{4F}{\rho\Omega^2}\right)\right) \tag{4.22}$$

Figure 4.5 shows as an example the power spectrum of the electron radiation spectrum (i.e., A_c^2) versus the dimensionless radiation frequency Δ/Ω for the case where $4F/(\rho\Omega) = 0.1$. It is seen that the most intense component in the spectrum is at the frequency Δ approximately equal to, but slightly less than Ω. It is also seen that the laser modulation of the primary frequency of the electron rotation results in a series of relatively small satellites of the primary spectral component.

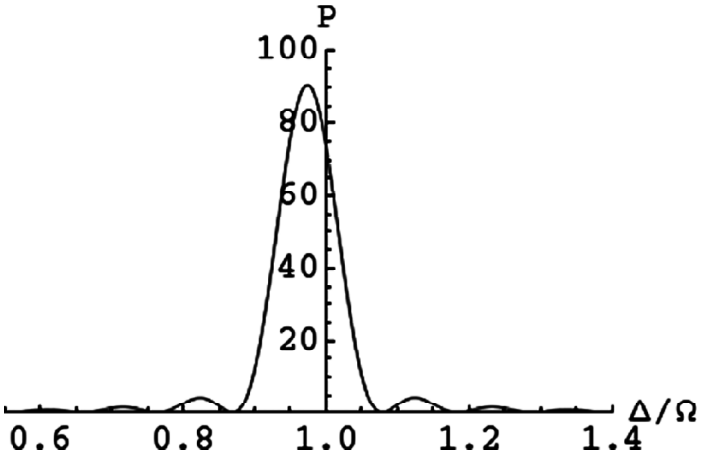

Figure 4.5: The power spectrum of the electron radiation *P* (in arbitrary units) versus the dimensionless radiation frequency Δ/Ω for the case where $4F/(\rho\Omega) = 0.1$. Here Ω is the frequency of the electron radiation at the absence of the laser field. A certain width is assigned to all spectral components to display a continuous spectral line profile

The red shift of the primary spectral component can be calculated analytically as follows. Since φ-motion is rapid, we can average the Hamiltonian in (4.16) with respect to time. Integrating (4.20) with the initial condition $d\theta/dt = \Omega$, we get

$$\Omega^2 - \left(\frac{d\theta}{dt}\right)^2 = \frac{4F}{\rho}\sin^2\frac{\theta}{2} \tag{4.23}$$

By averaging this equation with respect to time, we obtain

$$\Omega^2 - \left\langle \frac{d\theta}{dt} \right\rangle^2 = \frac{2F}{\rho} \tag{4.24}$$

Thus, the φ-momentum term in the Hamiltonian (4.16) becomes

$$\left\langle \frac{p_\varphi^2}{\rho^2} \right\rangle = \rho^2 \left\langle \left(\frac{d\theta}{dt} \right)^2 \right\rangle = \rho^2 \Omega^2 \left(1 - \frac{2F}{\rho\omega^2} \right) \tag{4.25}$$

The last term in the Hamiltonian from (4.16) vanishes after the time averaging so that the time-averaged Hamiltonian depends only on ρ- and *z*-coordinates and their corresponding momenta. The result is the following quasi-stationary Hamiltonian with no explicit time dependence:

$$H = \frac{1}{2}(p_\rho^2 + p_z^2) - \frac{Z}{\sqrt{\rho^2 + z^2}} - \frac{Z'}{\sqrt{\rho^2 + (R-z)^2}} + \frac{1}{2}\rho^2\Omega^2 - \rho F \tag{4.26}$$

Introducing the scaled quantities

$$w = \frac{z}{R}, \quad v = \frac{\rho}{R}, \quad f = \frac{FR^2}{Z}, \quad \sigma = \Omega\sqrt{\frac{R^3}{Z}} \tag{4.27}$$

and using the Hamilton equations, we obtain the following two differential equations of motion:

$$-\ddot{w} = \frac{w}{(w^2 + v^2)^{3/2}} - \frac{b(1-w)}{((1-w)^2 + v^2)^{3/2}} \tag{4.28}$$

$$-\ddot{v} = v\left(\frac{1}{(w^2 + v^2)^{3/2}} - \frac{b}{((1-w)^2 + v^2)^{3/2}} + \sigma^2 \right) - f \tag{4.29}$$

(the dot above the letter indicates the differentiation by the scaled time $\tau = t\,(Z/R^3)^{1/2}$).

In this section we consider these Rydberg quasimolecules in circular (not helical) states, so that the plane of the electron orbit has a stationary position on the internuclear axis. Therefore, the right-hand side of (4.28) vanishes and the relationship between *w* and *v* becomes the same as given by (4.4). This makes the scaled radius of the orbit *v* a constant as well.

Since the angular momentum is $L = \Omega\rho^2$ for a stationary circular orbit, the averaging of the φ-momentum in (4.25) is equivalent to changing *L* for $L(1 - F\rho^3/L^2)$. Using scaled units and the relationship $L = \Omega\rho^2$, we find out that the case of the circularly-polarized laser field is equivalent to a field-free case, but with an effective frequency Ω given by the substitution:

$$\Omega \to \Omega(1 - \kappa(\gamma) f) \tag{4.30}$$

where

$$\kappa(\gamma) = \frac{\gamma^6(\gamma^3 - 1)^{3/2}(\gamma^4 - b^{2/3})^{3/2}}{(\gamma^3 + 1)^{11/2}(b^{2/3}\gamma^2 - 1)^3} \tag{4.31}$$

The quantity $\Omega\kappa(\gamma) f$ is the red shift of the primary spectral component. This result is valid as long as the relative correction $\kappa(\gamma) f$ to the unperturbed angular frequency Ω of the electron remains relatively small. Figures 4.6 and 4.7

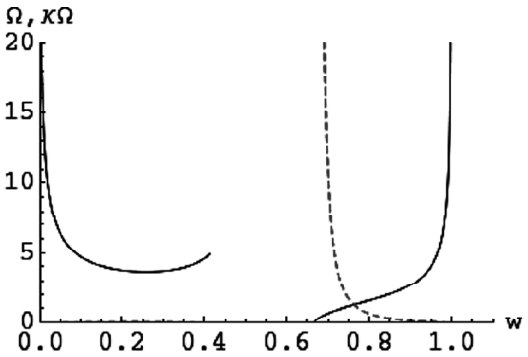

Figure 4.6: Dependence of the unperturbed angular frequency Ω of the electron (solid curve, two branches) and of the correction Ωκ(γ) *f* for *f* = 1 (dashed curve) on the scaled coordinate *w* along the internuclear axis of the Rydberg quasimolecule

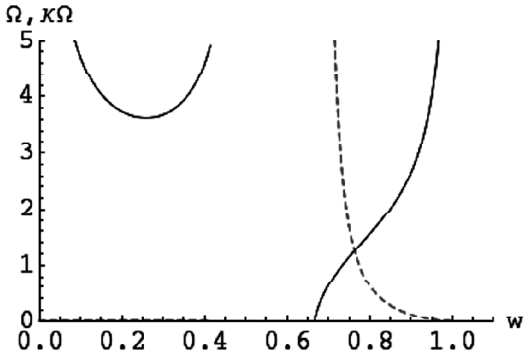

Figure 4.7: The same as in Fig. 4.6, but with better visible details in the region of the right branch of Ω(*w*)

illustrate the situation for the case where the ratio of the nuclear charges is $b = 2$. On the horizontal axis is the scaled coordinate w, i.e., the scaled coordinate along the internuclear axis of the Rydberg quasimolecule. The solid curve, having two branches, shows the unperturbed angular frequency Ω of the electron. The dashed curve shows the correction $\Omega\kappa(\gamma)\, f$. It is seen that the correction remains relatively small for the entire left branch of Ω and for a significant part of the right branch of Ω. (Figures 4.6 and 4.7 differ only by the range of the vertical scale, so that Fig. 4.6 allows to see more clearly the region where the solid and dashed curves intersect and the region of validity of the results for the right branch of Ω.) Physically, the left branch corresponds to the situation where the electron is primarily bound by the charge Z. The region of the right branch, where the correction is relatively small, physically corresponds to the situation where the electron is primarily bound by the charge Z'.

4.4. Conclusions

While studying diatomic Rydberg quasimolecules under a laser field that is linearly-polarized along the internuclear axis, we found an analytical solution for the stable helical motion of the electron valid for wide ranges of the laser field strength and frequency. Namely, the linearly-polarized laser field makes the motion in the $z\rho$-space to be forced oscillations at the frequency of the laser field. We also found resonances, corresponding to a laser-induced unstable motion of the electron, that result in the destruction of the helical states. For the situation where such Rydberg quasimolecules are under a circularly-polarized field, polarization plane being perpendicular to the internuclear axis, we found an analytical solution for circular Rydberg states valid for wide ranges of the laser field strength and frequency.

We showed that both under the linearly-polarized laser field and under the circularly-polarized laser field, in the electron radiation spectrum in the addition to the primary spectral component at (or near) the unperturbed revolution

frequency of the electron, there appear satellites. We found that for the case of the linearly-polarized laser field, the intensities of the satellites are proportional to the squares of the Bessel functions $J_q^2(s)$, (q = 1, 2, 3, …), where s is proportional to the laser field strength. As for the case of the circularly-polarized field, we demonstrated that there is a red shift of the primary spectral component – the shift linearly proportional to the laser field strength.

Under a laser field of a known strength, in the case of the linear polarization the observation of the satellites would be the confirmation of the helical electronic motion in the Rydberg quasimolecule, while in the case of the circular polarization the observation of the red shift of the primary spectral component would be the confirmation of the specific type of the phase modulation of the electronic motion described by (4.21). Conversely, if the laser field strength is unknown, both the relative intensities of the satellites and the red shift of the primary spectral component could be used for measuring the laser field strength.

Finally it should be noted that in paper [4.5] we generalized the above study by replacing the proton in μpe quasimolecule by a fully-stripped ion of a nuclear charge $Z > 1$. We showed that in this case, just as in the above case of $Z = 1$, the muonic motion can represent a rapid subsystem while the electronic motion can represent a slow subsystem. For this to be valid, the ratio of the muonic and electronic angular momenta should be slightly greater than in the case of $Z = 1$. We demonstrated that the binding energies of the muon for $Z > 1$ are much greater than for $Z = 1$ at any finite value of the nucleus-electron distance. Finally we showed that the red shift of the spectral lines emitted by the muon (compared to the spectral lines of the corresponding muonic hydrogenlike ion of the nuclear charge Z) decreases as Z increases. However, the relative red shift remains within the spectral resolution of available spectrometers at least up to $Z = 5$. Observing this red shift should be one of the ways to detect the formation of the quasimolecules μZe.

5. ATTACHMENT OF AN ELECTRON BY MUONIC HYDROGEN ATOMS: CIRCULAR STATES

5.1. Introduction

Studies of muonic atoms and molecules, where one of the electrons is substituted by the heavier lepton μ^-, have several applications. The first one is muon-catalyzed fusion (see, e.g., [5.1-5.3] and references therein). When a muon replaces the electron either in the dde-molecule (D_2^+), which becomes the $dd\mu$-molecule, or in the dte-molecule, which becomes the $dt\mu$-molecule, the equilibrium internuclear distance becomes about 200 times smaller. At such small internuclear distances, the fusion can occur with a significant probability, which has been observed in $dd\mu$ or even with a higher rate in $dt\mu$ [5.1-5.3]. The second application is a laser-control of nuclear processes. This has been discussed in the context of the interaction of muonic molecules with superintense laser fields [5.4]. Another application is a search for strongly interacting massive particles (SIMPs) proposed as dark matter candidates and as candidates for the lightest supersymmetric particle (see, e.g., [5.5] and references therein). SIMPs could bind to the nuclei of atoms, and would manifest themselves as anomalously heavy isotopes of known elements. By greatly increasing the nuclear mass, the presence of a SIMP in the nucleus effectively eliminates the well-known reduced mass correction in a hydrogenic atom. Muonic atoms are better candidates (than electronic atoms) for observing this effect because the muon's much larger mass (compared to the electron) amplifies the reduced mass correction [5.5]. This may be detectable in astrophysical objects [5.5].

Another line of research is studies of the negative ion of hydrogen H^-, which can be also denoted as epe-system (electron-proton-electron), constitute an important line of research in atomic physics and astrophysics. It has only one bound state – the ground state having a relatively small bound energy of approximately 0.75 eV. This epe-system exhibits rich physics. Correlations between the two electrons are strong already in the ground state. With long-range Coulomb interactions between all three pairs of particles, the dynamics is particularly subtle in a range of energies 2 – 3 eV on either side of the threshold for break-up into proton + electron + electron at infinity [5.6]. There are strong correlations in energy, angle, and spin degrees of freedom, so that perturbation theory and other similar methods fail [5.6]. Experimental studies of H^- provided a testing ground for the theory of correlated multielectron systems. Compared to the helium atom, the structure of H^- is even more strongly influenced by interelectron repulsion because the nuclear attraction is smaller for this system [5.7]. In addition to the above

fundamental importance, the rich physics of H^- is also important in studies of the ionosphere's *D*-layer of the Earth atmosphere, the atmosphere of the Sun and other stars, and in development of particle accelerators [5.6].

In this chapter we combine the above two lines of research: studies of muonic atoms/molecules and studies of negative hydrogen ion. Namely, we consider whether a muonic hydrogen atom can attach an electron and become a muonic negative hydrogen ion, i.e. μpe-system. Specifically, we study a possibility of circular states in such system. We show that the muonic motion can represent a rapid subsystem, while the electronic motion can represent a slow subsystem – the result that might seem counterintuitive.

First, we find analytically classical energy terms for the rapid subsystem at the frozen slow subsystem, i.e., for the quasimolecule where the muon rotates around the axis connecting the immobile proton and the immobile electron. The meaning of classical energy terms is explained below. We demonstrate that the muonic motion is stable. We also conduct the analytical relativistic treatment of the muonic motion.

Then we unfreeze the slow subsystem and analyse a slow revolution of the axis connecting the proton and electron. We derive the condition required for the validity of the separation into the rapid and slow subsystems.

Finally we show that the spectral lines, emitted by the muon in the quasimolecule μpe, experience a red shift compared to the corresponding spectral lines that would have been emitted by the muon in a muonic hydrogen atom (in the μp-subsystem). Observing this red shift should be one of the ways to detect the formation of such muonic negative hydrogen ions.

As for physical processes leading to the formation of muonic-electronic negative hydrogen ions, one of the processes could be the following:

$$e + \mu p \rightarrow \mu pe$$

(which sometimes might be followed by the decay $\mu pe \rightarrow \mu + pe$). Such formation of the μpe-systems was discussed, e.g., in paper [5.8], where these systems were called resonances. The theoretical approach based on the separation of rapid and slow subsystems requires in this case the muon to be in a state of a high angular momentum. Luckily, the experimental methods to create muonic hydrogen atoms μp (necessary for the above reaction) lead to the muon being in a highly-excited state (see, e.g., review [5.9] and paper [5.10]). We also mention paper [5.11] where it has been shown, in particular, that the distribution of the muon principal quantum number in muonic hydrogen atoms peaks at larger and larger values with the increase of the energy of the muon incident on electronic hydrogen atoms.

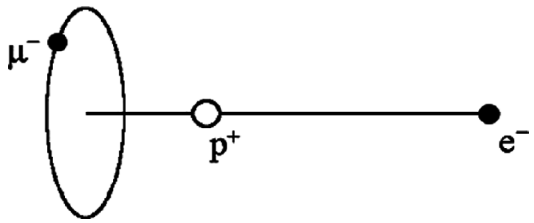

Figure 5.1: A muon rotating in a circle perpendicular to and centered at the axis connecting the proton and the electron

5.2. Analytical Solution for Classical Energy Terms of the Rapid Subsystem

We consider a quasimolecule where a muon rotates in a circle perpendicular to and centered at the axis connecting a proton and an electron – see Fig. 5.1. As we show below, in this configuration the muon may be considered the rapid subsystem while the proton and electron will be the slow subsystem, which essentially reduces the problem to the two stationary Coulomb center problem, where the effective stationary "nuclei" will be the proton and electron. The straight line connecting the proton and electron will be called here "internuclear" axis. We use the atomic units in this study.

Because of the difference of muon and electron masses, the muon-proton separation is much smaller than the electron-proton separation. Therefore, it should be expected that the spectral lines, emitted by this system, would be

relatively close to the spectral lines emitted by muonic hydrogen atoms. In other words, the presence of the electron should result in a relatively small shift of the spectral lines (compared to muonic hydrogen atoms); however, this shift would be an important manifestation of the formation of the quasimolecule μpe.

A detailed classical analytical solution of the two stationary Coulomb center problem, where an electron revolves around nuclei of charges Z and Z', has been presented in papers [1.18, 1.19]. We base our results in part on the results obtained therein.

The Hamiltonian of the rotating muon is

$$H = \frac{1}{2m}\left(p_z^2 + p_\rho^2 + \frac{p_\varphi^2}{\rho^2} \right) - \frac{Z}{\sqrt{z^2+\rho^2}} - \frac{Z'}{\sqrt{(R-z)^2+\rho^2}} \tag{5.1}$$

where m is the mass of the muon (in atomic units $m = 206.7682746$), Z and Z' are the charges of the effective nuclei (in our case, $Z = 1$ and $Z' = -1$), R is the distance between the effective nuclei, (ρ, φ, z) are the cylindrical coordinates, in which Z is at the origin and Z' is ar $z = R$, and (p_ρ, p_φ, p_z) are the corresponding momenta of the muon.

Since φ is a cyclic coordinate, the corresponding momentum is conserved:

$$| p_\varphi | = \text{const} = L \tag{5.2}$$

With this substituted into (5.1), we obtain the Hamiltonian for the z- and ρ-motions

$$H_{z\rho} = \frac{p_z^2 + p_\rho^2}{2} + U_{eff}(z, \rho) \tag{5.3}$$

where an effective potential energy is

$$U_{eff}(z, \rho) = \frac{L^2}{2m\rho^2} - \frac{Z}{\sqrt{z^2+\rho^2}} - \frac{Z'}{\sqrt{(R-z)^2+\rho^2}} \tag{5.4}$$

Because in a circular state $p_z = p_\rho = 0$, the total energy $E(z, \rho) = U_{eff}(z, \rho)$.

With $Z = 1$, $Z' = -1$ and the scaled quantities

$$w = \frac{z}{R}, \quad v = \frac{\rho}{R}, \quad \varepsilon = -ER, \quad \ell = \frac{L}{\sqrt{mR}}, \quad r = \frac{mR}{L^2} \tag{5.5}$$

we obtain the scaled energy ε of the muon:

$$\varepsilon = \frac{1}{\sqrt{w^2+v^2}} - \frac{1}{\sqrt{(1-w)^2+v^2}} - \frac{\ell^2}{2v^2} \tag{5.6}$$

The equilibrium condition with respect to the scaled coordinate w is $\partial\varepsilon/\partial w = 0$; the result can be brought to the form:

$$\frac{((1-w)^2+v^2)^{3/2}}{(w^2+v^2)^{3/2}} = \frac{w-1}{w} \tag{5.7}$$

Since the left-hand side of (5.7) is positive, the right-hand side must also be positive: $(w-1)/w > 0$. Consequently, the allowed ranges of w here are $-\infty < w < 0$ and $1 < w < +\infty$. This means that equilibrium positions of the center of the muon orbit could exist (judging only by the equilibrium with respect to w) either beyond the proton or beyond the electron, but there are no equilibrium positions between the proton and electron.

Solving (5.7) for v^2 and denoting $v^2 = p$, we obtain:

$$p(w) = w^{2/3}(w-1)^{2/3}(w^{2/3} + (w-1)^{2/3}) \tag{5.8}$$

The equilibrium condition with respect to the scaled coordinate v is $\partial\varepsilon/\partial v = 0$, which yields

$$\ell^2 = p^2\left(\frac{1}{(w^2+p)^{3/2}} - \frac{1}{((1-w)^2+p)^{3/2}}\right) \tag{5.9}$$

Since the left-hand side of (5.9) is positive, the right-hand side must be also positive. This entails the relation $w^2 + p < (1-w)^2 + p$, which simplifies to $2w - 1 < 0$, which requires $w < 1/2$.

Thus, the equilibrium with respect to both w and v is possible only in the range $-\infty < w < 0$, while in the second range, $1 < w < +\infty$ (derived from the equilibrium with respect to w only) there is no equilibrium with respect to v.

From the last two relations in (5.5), we find $r = 1/\ell^2$; thus

$$r = p^{-2}\left(\frac{1}{(w^2+p)^{3/2}} - \frac{1}{((1-w)^2+p)^{3/2}}\right)^{-1} \tag{5.10}$$

where p is given by (5.8). Therefore, the quantity r in (5.10) is the scaled "internuclear" distance dependent on the scaled internuclear coordinate w.

Now we substitute the value of ℓ from (5.9), as well as the value of p from (5.8) into (5.6), obtaining $\varepsilon(w)$ – the scaled energy of the muon dependent on the scaled internuclear coordinate w. Since $E = -\varepsilon/R$ and $R = rL^2/m$, then $E = -(m/L^2)\varepsilon_1$ where $\varepsilon_1 = \varepsilon/r$. The parametric dependence $\varepsilon_1(r)$ will yield the energy terms.

The form of the parametric dependence $\varepsilon_1(r)$ can be significantly simplified by introducing a new parameter $\gamma = (1 - 1/w)^{1/3}$, as was shown in Section 1 starting from (1.10). The region $-\infty < w < 0$ corresponds to $1 < \gamma < \infty$. The parametric dependence will then have the following form:

$$\varepsilon_1(\gamma) = \frac{(1-\gamma)^4(1+\gamma^2)^2}{2(1-\gamma+\gamma^2)^2(1+\gamma^2+\gamma^4)} \tag{5.11}$$

$$r(\gamma) = \frac{(1+\gamma^2+\gamma^4)^{3/2}}{\gamma(1+\gamma^2)^2} \tag{5.12}$$

Classical energy terms given by the parametric dependence of the scaled energy $\varepsilon_1 = (L^2/m)\,E$ on the scaled internuclear distance $r = (m/L^2)\,R$ are presented in Fig. 5.2.

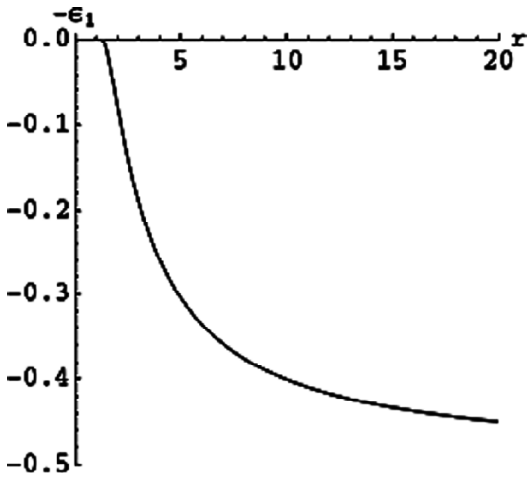

Figure 5.2: Classical energy terms: the scaled energy $-\varepsilon_1 = (L^2/m)\,E$ versus the scaled internuclear distance $r = (m/L^2)\,R$.

Fig. 5.2 actually contains two coinciding energy terms: there is a double degeneracy with respect to the sign of the projection of the muon angular momentum on the internuclear axis. We remind the readers that L is the absolute value of this projection – in accordance to its definition in (5.2).

The minimum value of R, corresponding to the point where the term starts, can be found from (5.12). The term starts at $w = -\infty$, which corresponds to $\gamma = 1$; taking the value of (5.12) at this point, we find

$$R_{\min} = \frac{3^{3/2}}{4}\frac{L^2}{m} \tag{5.13}$$

With the value of $m = 206.7682746$, (5.13) yields $R = 0.00628258\ L^2$.

The following note might be useful once again. The plot in Fig. 5.1 represents two degenerate classical energy terms of "the same symmetry". (In physics of diatomic molecules, the terminology "energy terms of the same symmetry" means the energy terms of the same projection of the angular momentum on the internuclear axis.) For a given R and L, the classical energy E takes only one *discrete* value. However, as L varies over a *continuous* set of values, so does the classical energy E (as it should be in classical physics).

The revolution frequency of the muon Ω is

$$\Omega = \frac{L}{m\rho^2} = \frac{L}{mR^2v^2} = \frac{L}{mR^2 p} \tag{5.14}$$

in accordance with the previously introduced notation $p = v^2 = (\rho/R)^2$. Since $R = L^2 r/m$ (see (5.5)), then (5.14) becomes $\Omega = (m/L^3)\, f$, where $f = 1/(pr^2)$. Using (5.12) for $r(\gamma)$ and (5.8) for $p(w)$ with the substitution $w = 1/(1-\gamma^3)$, where $\gamma > 1$, we finally obtain:

$$\Omega = \frac{m}{L^3}\, f(\gamma), \qquad f(\gamma) = \frac{(1+\gamma^2)^3(1-\gamma^3)^2}{(1+\gamma^2+\gamma^4)^3} \tag{5.15}$$

where $f(\gamma)$ is the scaled muon revolution frequency. Fig. 5.3 shows the scaled muon revolution frequency $f = (L^3/m)\,\omega$ versus the scaled internuclear distance $r = (m/L^2)R$.

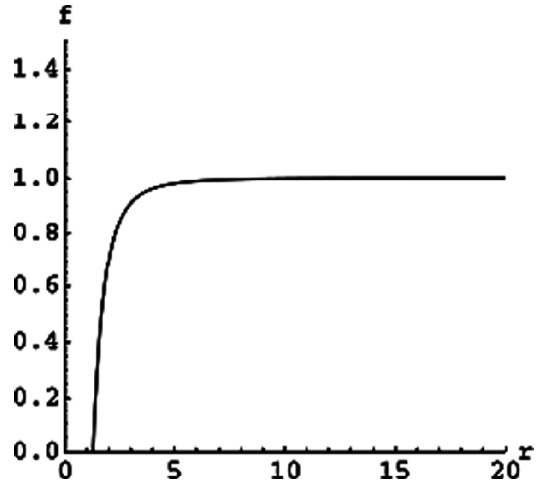

Figure 5.3: The scaled muon revolution frequency $f = (L^3/m)\,\Omega$ versus the scaled internuclear distance $r = (m/L^2)R$

It is seen that for almost all values of the scaled internuclear distance $r = (m/L^2)R$, the scaled muon revolution frequency $f = (L^3/m)\,\Omega$ is very close to its maximum value $f_{\max} = 1$, corresponding to large values of R. (The quantity $f_{\max}$ can be easily found from (15) given that large values of R correspond to $\gamma \gg 1$ and that this limit yields $f_{\max} = 1$.) In other words, for almost all values of R, the muon revolution frequency Ω is very close to its maximum value

$$\Omega_{\max} = \frac{m}{L^3} \tag{5.16}$$

In Sect. 5.3, we will compare the muon revolution frequency with the corresponding frequency of the electronic motion and derive the condition of validity of the separation into rapid and slow subsystems.

To analyse the stability of the muon motion, corresponding to the degenerate classical energy terms, while considering a classical circular motion of a charged particle (which was the electron in [1.19]) in the field of two stationary Coulomb centers, using the same notation as in this chapter, it was shown [1.19] that the frequencies of small oscillations of the scaled coordinates w and v of the circular orbit around its equilibrium position are given by

$$\omega_{\pm} = \frac{1}{(w^2 + p)^{3/4}} \sqrt{\frac{1}{1-w} \pm \frac{3w}{Q}} \tag{5.17}$$

where

$$Q = \sqrt{(w^2 + p)((1-w)^2 + p)} \tag{5.18}$$

These oscillations are in the directions (w', v') obtained by rotating the (w, v) coordinates by the angle α:

$$\delta w' = \delta w \cos\alpha + \delta v \sin\alpha, \qquad \delta v' = -\delta w \sin\alpha + \delta v \cos\alpha \tag{5.19}$$

where the "δ" symbol stands for the small deviation from equilibrium. The angle α is determined by the following relation:

$$\alpha = \frac{1}{2} \operatorname{arctg} \frac{(1-2w)\sqrt{p}}{w(1-w) + p} \tag{5.20}$$

The quantity Q in (5.18) is always positive since it contains the squares of the coordinates. From (5.17) it is seen that the condition for both frequencies to be real is

$$\frac{1}{1-w} \geq \frac{3w}{Q} \tag{5.21}$$

For the frequency ω_- to be real, (5.17) requires $Q \geq 3w(1-w)$. For any $w < 0$ (which is the allowed range of w), this inequality is satisfied: the left-hand side is always positive while the right-hand side is always negative.

For the frequency ω_+ to be real, the following function $F(w)$ must be positive (in accordance with (5.17) and (5.18)):

$$F(w) = (w^2 + p)((1-w)^2 + p) - 9w^2(1-w)^2 \tag{5.22}$$

After replacing w by $\gamma = (1 - 1/w)^{1/3}$, (5.22) becomes

$$F(\gamma) = \frac{\gamma^2(\gamma^2 - 1)^2(1 + 4\gamma^2 + \gamma^4)}{(\gamma^3 - 1)^4} \tag{5.23}$$

Since the allowed range of $w < 0$ corresponds to $\gamma > 1$, it is seen that $F(\gamma)$ is always positive.

Thus, the corresponding classical energy terms corresponds to the stable motion.

5.3. Electronic Motion and the Validity of the Scenario

Now we unfreeze the slow subsystem and analyse a slow revolution of the axis connecting the proton and electron, the electron executing a circular orbit. In accordance with the concept of separating rapid and slow subsystems, the rapid subsystem (the revolving muon) follows the adiabatic evolution of the slow subsystem. This means that the slow subsystem can be treated as a modified "rigid rotator" consisting of the electron, the proton, and the ring, over which the muon charge is uniformly distributed, all distances within the system being fixed (see Fig. 5.1).

The potential energy of the electron in atomic units (with the angular-momentum term) is

$$E_e = \frac{M^2}{2R^2} - \frac{1}{R} + \frac{1}{\sqrt{\rho^2 + (R-z)^2}} \tag{5.24}$$

where M is the electronic angular momentum. Its derivative by R must vanish at equilibrium, which yields

$$\frac{dE_e}{dR} = -\frac{M^2}{R^3} + \frac{1}{R^2} - \frac{R-z}{(\rho^2 + (R-z)^2)^{3/2}} = 0 \tag{5.25}$$

which gives us the value of the scaled angular momentum

$$\ell_e = \frac{M}{\sqrt{R}} \tag{5.26}$$

corresponding to the equilibrium:

$$\ell_e^2 = 1 - \frac{1-w}{((1-w)^2 + p)^{3/2}} \tag{5.27}$$

where the scaled quantities w, p of the muon coordinates are defined in (5.5). Using the muon equilibrium condition from (5.7) with v^2 denoted as p, we can represent (5.27) in the form

$$\ell_e^2 = 1 + \frac{w}{(w^2 + p)^{3/2}} \tag{5.28}$$

After replacing w by $\gamma = (1 - 1/w)^{1/3}$, we obtain

$$\ell_e(\gamma) = \sqrt{1 - \frac{(1-\gamma)^2\sqrt{1+\gamma+\gamma^2}}{(1-\gamma+\gamma^2)^{3/2}}} \tag{5.29}$$

The electron revolution frequency is $\omega = M/R^2 = \ell_e(\gamma)/R^{3/2}$ given that $M = \ell_e(\gamma)R^{1/2}$ in accordance with (5.26). Since $R = L^2 r(\gamma)/m$ (see (5.5)) with $r(\gamma)$ given by (5.12), then from $\omega = \ell_e(\gamma)/R^{3/2}$ we obtain

$$\omega = \frac{m^{3/2}\ell_e(\gamma)}{L^3 r^{3/2}(\gamma)} \tag{5.30}$$

From (5.15) and (5.30) we find the following ratio of the muon and electron revolution frequencies:

$$\frac{\Omega}{\omega} = \frac{1}{\sqrt{m}} \frac{f(\gamma) r^{3/2}(\gamma)}{\ell_e(\gamma)} \tag{5.31}$$

where $f(\gamma)$ is given in (5.15).

In addition to the above relation $R = L^2 r(\gamma)/m$, the same quantity R can be expressed from (5.26) as $R = M^2/\ell_e^2(\gamma)$. Equating the right-hand sides of these two expressions, we obtain the equality $L^2 r(\gamma)/m = M^2/\ell_e^2(\gamma)$, from which it follows:

$$\frac{L}{M} = \frac{\sqrt{m}}{\ell_e(\gamma)\sqrt{r(\gamma)}} \tag{5.32}$$

The combination of (5.31) and (5.32) represents an analytical dependence of the ratio of the muon and electron revolution frequencies Ω/ω versus the ratio of the muon and electron angular momenta L/M via the parameter γ as the latter varies from 1 to ∞. This dependence is presented in Fig. 5.4.

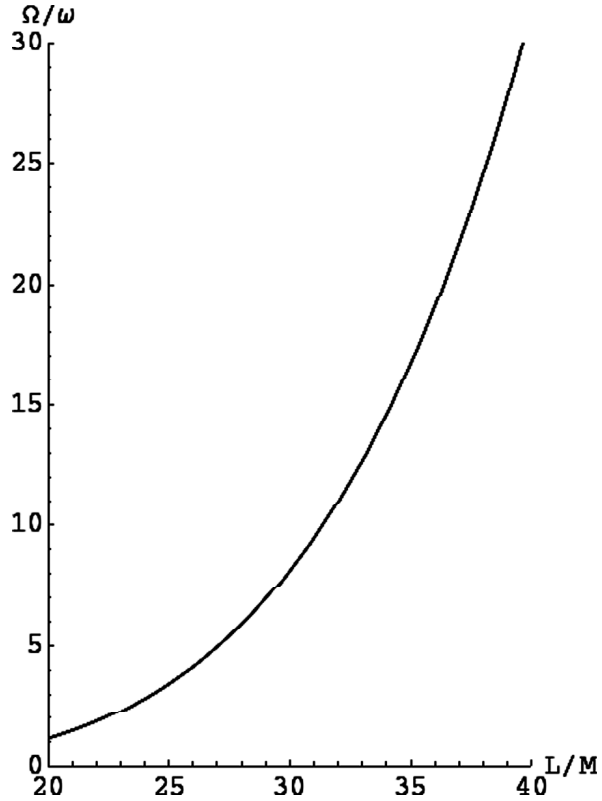

Figure 5.4: The ratio of the muon and electron revolution frequencies Ω/ω versus the ratio of the muon and electron angular momenta L/M

For the separation into the rapid and slow subsystems to be valid, the ratio of frequencies Ω/ω should be significantly greater than unity. From Fig. 5.4 it is seen that this requires the ratio of angular momenta L/M to be noticeably greater than 20.

There is another validity condition to be checked for this scenario. Namely, the revolution frequency Ω of the muon must also be much greater than the inverse lifetime of the muon $1/T_{\text{life}}$, where $T_{\text{life}} = 2.2\ \mu\text{s} = 0.91 \times 10^{11}$ a.u.: $\Omega T_{\text{life}} >> 1$. Since for almost all values of R, the muon revolution frequency Ω is very close to its maximum value $\Omega_{\max} = m/L^3$, as shown in Sect. 5.2, then the second validity condition can be estimated as $(m/L^3)T_{\text{life}} >> 1$, from which it follows

$$L << L_{\max} = (mT_{\text{life}})^{1/3} = 26600 \tag{5.33}$$

(we remind that $m = 206.7682746$ in atomic units). So, the second validity condition is fulfilled for any practically feasible value of the muon angular momentum L.

Thus, for the ratio of angular momenta L/M noticeably greater than 20, we deal here with a muonic quasimolecule where the muon rapidly rotates about the axis connecting the proton and electron following a relatively slow rotation of this axis.

5.4. Red Shift of Spectral lines Compared to Muonic Hydrogen Atoms

The muon, rotating in a circular orbit at the frequency $\Omega(R)$, should emit a spectral line at this frequency. The maximum value $\Omega_{max} = m/L^3$ corresponds to the frequency of spectral lines emitted by the muonic hydrogen atom (by the μp-subsystem). For the equilibrium value of the proton-electron separation – just as for almost all values of R – the frequency Ω is slightly smaller than Ω_{max}. Therefore, the spectral lines, emitted by the muon in the quasimolecule μpe, experience a red shift compared to the corresponding spectral lines that would have been emitted by the muon in a muonic hydrogen atom. The relative red shift δ is defined as follows

$$\delta = \frac{\lambda - \lambda_0}{\lambda_0} = \frac{\Omega_{max} - \Omega}{\Omega} \tag{5.34}$$

where λ and λ_0 are the wavelength of the spectral lines for the quasimolecule μpe and the muonic hydrogen atom, respectively. Using (5.15), the relative red shift can be represented in the form

$$\delta(\gamma) = \frac{1}{f(\gamma)} - 1 \tag{5.35}$$

where $f(\gamma)$ is given in (5.15).

The combination of (5.35) and (5.32) represents an analytical dependence of the relative red shift δ on the ratio of the muon and electron angular momenta L/M via the parameter γ as the latter varies from 1 to ∞. Figure 5.5 presents the logarithmic dependence (in the figures below, "Log δ" stands for "$\log_{10} \delta$") of δ on $L/(m^{1/2} M)$". In this form the dependence is "universal", i.e., valid for different values of the mass m: for example, it is valid also for the quasimolecule πpe where there is a pion instead of the muon. Figure 5.6 presents the dependence of δ on L/M

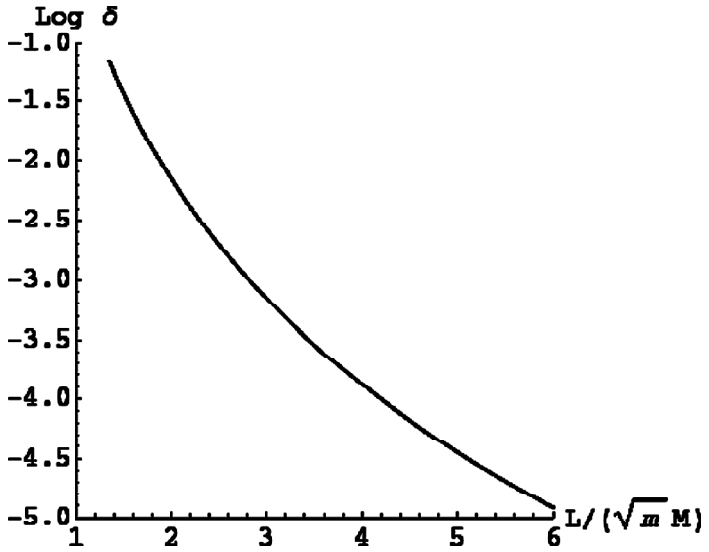

Figure 5.5: Universal dependence of the relative red shift δ of the spectral lines of the quasimolecule μpe (or πpe) on $L/(m^{1/2}M)$, which is the ratio of the muon and electron angular momenta L/M divided by the square root of the mass m of the muon or pion

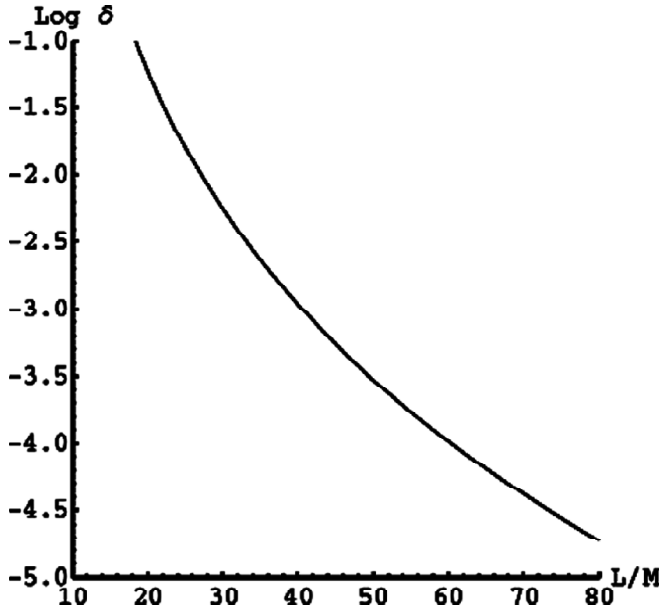

Figure 5.6: Dependence of the relative red shift δ of the spectral lines of the quasimolecule μ*pe* on the ratio of the muon and electron angular momenta *L*/*M*

specifically for the quasimolecule μ*pe*.

It is seen that is the relative red shift of the spectral lines is well within the spectral resolution $\Delta\lambda_{res}/\lambda$ of available spectrometers: $\Delta\lambda_{res}/\lambda \sim (10^{-4} - 10^{-5})$ as long as the ratio of the muon and electron angular momenta $L/M < 80$. Thus, this red shift can be observed and this would be one of the ways to detect the formation of such muonic negative hydrogen ions.

Figure 5.7 presents the dependence of the relative red shift δ on the ratio of the muon and electron revolution

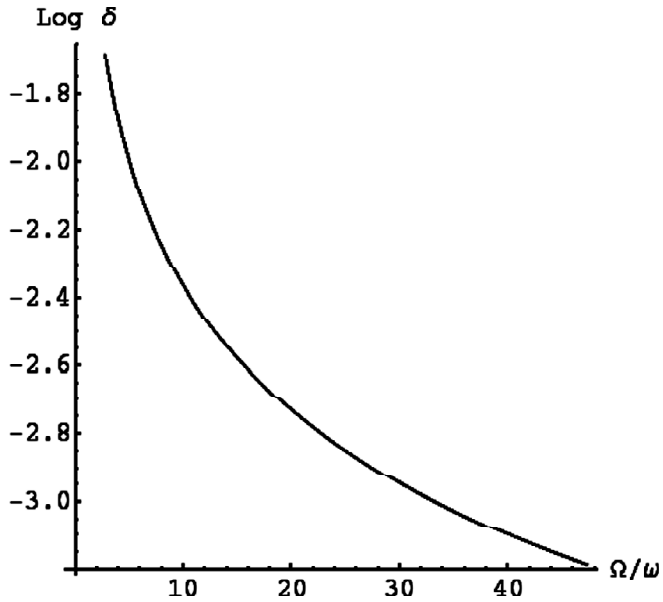

Figure 5.7: Dependence of the relative red shift δ on the ratio of the muon and electron revolution frequencies Ω/ω

frequencies Ω/ω. It is seen that the relative red shift decreases as the ratio of the muon and electron revolution frequencies increases, but it remains well within the spectral resolution $\Delta\lambda_{res}/\lambda$ of available spectrometers.

5.5. Conclusions

We studied whether a muonic hydrogen atom can attach an electron, the muon and the electron being in circular states. We showed that it is indeed possible for a muonic hydrogen atom to attach an electron and to become a muonic negative hydrogen ion. We demonstrated that in this case, the muonic motion can represent a rapid subsystem while the electronic motion can represent a slow subsystem – the result that might seem counterintuitive. In other words, the muon rapidly revolves in a circular orbit about the axis connecting the proton and electron while this axis slowly rotates following a relatively slow electronic motion.

We used a classical analytical description to find the energy terms of such a system, i.e., dependence of the energy of the muon on the distance between the proton and electron. We found that there is a double-degenerate energy term. We demonstrated that it corresponds to a stable motion. We also conducted the analytical relativistic treatment of the muonic motion, which is presented in Appendix 5A. It was found that the relativistic corrections are relatively small. Their relative value is $\sim 1/(cL)^2 \sim 0.5 \times 10^{-4}/L^2$ (we remind the readers that here $c = 137.036$ is the speed of light in atomic units).

Then we unfroze the slow subsystem and analysed a slow revolution of the axis connecting the proton and electron. The slow subsystem can be treated as a modified "rigid rotator" consisting of the electron, the proton, and the ring, over which the muon charge is uniformly distributed, all distances within the system being fixed. We derived the condition required for the validity of the separation into the rapid and slow subsystems.

Finally we showed that the spectral lines, emitted by the muon in the quasimolecule μpe, experience a red shift compared to the corresponding spectral lines that would have been emitted by the muon in a muonic hydrogen atom (in the μp-subsystem). The relative values of this red shift, which is a "molecular" effect, are significantly greater than the resolution of available spectrometers and thus can be observed. Observing this red shift should be one of the ways to detect the formation of such muonic negative hydrogen ions.

APPENDIX 5A
RELATIVISTIC TREATMENT OF THE MUONIC MOTION

The Hamiltonian of the rotating muon is

$$H = c\sqrt{m^2c^2 + p_z^2 + p_\rho^2 + \frac{p_\varphi^2}{\rho^2}} - \frac{Z}{\sqrt{z^2+\rho^2}} - \frac{Z'}{\sqrt{(R-z)^2+\rho^2}} - mc^2 \qquad (5.A.1)$$

Since φ is a cyclic coordinate, the corresponding momentum is conserved:

$$\left| p_\varphi \right| = \text{const} = L \qquad (5.A.2)$$

With this substituted into (5.A.1) and taking into account that in a circular state, $p_z = p_\rho = 0$, we obtain the energy of the muon in a circular state

$$E = c\sqrt{m^2c^2 + \frac{L^2}{\rho^2}} - \frac{Z}{\sqrt{z^2+\rho^2}} - \frac{Z'}{\sqrt{(R-z)^2+\rho^2}} - mc^2 \qquad (5.A.3)$$

With $Z = 1$, $Z' = -1$ and the scaled quantities

$$w = \frac{z}{R}, \quad \nu = \frac{\rho}{R}, \quad \varepsilon = -ER, \quad \ell = \frac{L}{mcR}, \quad r = \frac{R}{L} \tag{5.A.4}$$

we obtain the scaled energy ε of the muon:

$$\varepsilon = \frac{1}{\sqrt{w^2 + \nu^2}} - \frac{1}{\sqrt{(1-w)^2 + \nu^2}} - mc^2 R\left(1 - \sqrt{1 + \frac{\ell^2}{\nu^2}}\right) \tag{5.A.5}$$

The equilibrium condition with respect to the scaled coordinate w is $\partial\varepsilon/\partial w = 0$, which yields

$$p(w) = w^{2/3}(w-1)^{2/3}(w^{2/3} + (w-1)^{2/3}) \tag{5.A.6}$$

where $p = \nu^2$.

The equilibrium condition with respect to the scaled coordinate ν is $\partial\varepsilon/\partial\nu = 0$, which yields:

$$\ell^2 = \frac{p^2}{mc^2 R}\sqrt{1 + \frac{\ell^2}{p}}\left(\frac{1}{(w^2 + p)^{3/2}} - \frac{1}{((1-w)^2 + p)^{3/2}}\right) \tag{5.A.7}$$

From the relation before last in (5.A.4), we find $R = L/(mc\ell)$. Substituting this in (5.A.7), we can solve it for ℓ and obtain:

$$\ell = \left(\frac{c^2 L^2}{p^4}\frac{1}{\left(\frac{1}{(w^2 + p)^{3/2}} - \frac{1}{((1-w)^2 + p)^{3/2}}\right)^2} - \frac{1}{p}\right)^{-1/2} \tag{5.A.8}$$

From the last two relations in (5.A.4), we find $r = 1/(mc\ell)$; thus

$$r = \frac{1}{mc}\sqrt{\frac{c^2 L^2}{p^4}\frac{1}{\left(\frac{1}{(w^2 + p)^{3/2}} - \frac{1}{((1-w)^2 + p)^{3/2}}\right)^2} - \frac{1}{p}} \tag{5.A.9}$$

where p is given by (5.A.6). Therefore, the quantity r in (5.A.9) is the scaled "internuclear" distance dependent on the scaled internuclear coordinate w for a given absolute value of the angular momentum projection on the internuclear axis L.

Now we substitute $R = L/(mc\ell)$ and the value of ℓ from (5.A.8), as well as the value of p from (5.A.6) into (5.A.5), obtaining $\varepsilon(w, L)$ – the scaled energy of the muon dependent on the scaled internuclear coordinate w for a given value of the angular momentum L. Since $E = -\varepsilon/R$ and $R = rL$, then $E = -\varepsilon_1/L$ where $\varepsilon_1 = \varepsilon/r$. The parametric dependence $E(R)$, where $E = -\varepsilon_1/L$ and $R = Lr$ will yield the energy terms for a given value of L.

After introducing the parameter $\gamma = (1 - 1/w)^{1/3}$, the parametric dependence takes the following form:

$$E(\gamma, L) = -mc^2\left(1 + \frac{1}{\sqrt{\sigma^6 - \tau}}\left(\frac{\tau}{\sigma\sqrt{1 + \gamma + \gamma^2}} - \sigma^3\right)\right) \tag{5.A.10}$$

$$R(\gamma, L) = \frac{L^2}{m} \frac{\sqrt{\sigma^6 - \tau}}{\gamma\sqrt{1+\gamma^2}} \tag{5.A.11}$$

where quantities σ and τ are defined as follows:

$$\sigma = \sqrt{\frac{1+\gamma^2+\gamma^4}{1+\gamma^2}}, \qquad \tau = \left(\frac{1-\gamma^3}{cL}\right)^2 \tag{5.A.12}$$

The revolution frequency of the muon is

$$\omega = \frac{mc^2}{L} \frac{\tau}{\sigma^6 - \tau} \sqrt{1 - \frac{\tau}{\sigma^6 - \tau}} \tag{5.A.13}$$

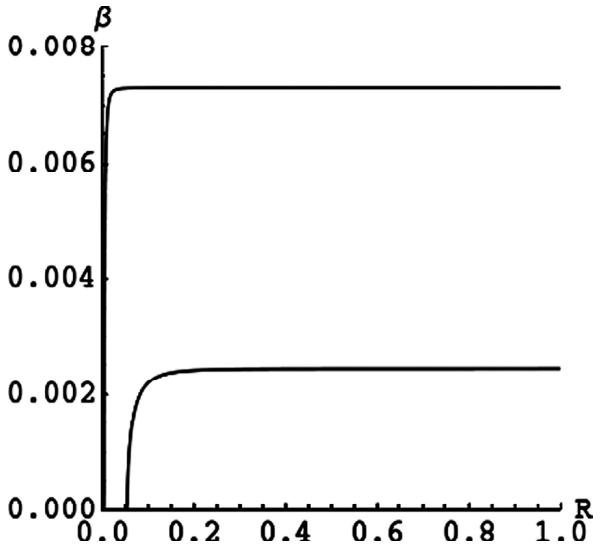

Figure 5.A1: The ratio β of the muon velocity to the speed of light versus the "internuclear" distance *R* (a.u.) for *L* = 1 (the upper curve) and *L* = 3 (the lower curve)

Let us check the degree of the relativity of the muon motion. Figure 5.A.1 shows the ratio β of the muon velocity to the speed of light versus the "internuclear" distance *R* for *L* = 1 and *L* = 3. It is seen that for all values of $R \approx n^2$ (n = 1, 2, 3, ...), this ratio is practically equal to some constant value β_{max}. It is easy to find that $\beta_{max} = 1/(cL) = 1/(137.036\, L)$ – since c = 137.036 in a.u.

It is interesting to compare the above β_{max} with the corresponding average value of β_e for the electron motion in hydrogen atoms: $\beta_e = 1/(cn)$. So, β_{max} for the muon motion differs from β_e for the electron motion in hydrogen atoms only by the substitution of the principal quantum number n of the electron by the angular momentum quantum number L of the muon.

Thus, even for L = 1 (for which β_{max} is the highest), the muon motion is only weakly-relativistic. The relativistic correction to the average frequency of the muon radiation is $\sim 1/(cL)^2$ (a.u.), where c = 137.036. Thus, the relative correction is insignificant even for $L \sim 1$ and it rapidly diminishes as L grows: for example, it is $\sim 10^{-5}$ for L = 3 and $\sim 10^{-7}$ for L = 15.

6. CONCLUSIONS OF THE REVIEW

In this work we studied classically two-Coulomb-center systems consisting of two nuclei of charges Z and Z' and an electron in the field of these nuclei in a circular or a helical state . These systems represent diatomic Rydberg quasimolecules encountered, e.g., in plasmas containing more than one kind of multicharged ions. Diatomic Rydberg quasimolecules are one of the most fundamental theoretical playgrounds for studying charge exchange. Charge exchange and crossings of corresponding energy levels that enhance charge exchange are strongly connected with problems of energy losses and of diagnostics in high temperature plasmas; besides, charge exchange is one of the most effective mechanisms for population inversion in the soft *x*-ray and *VUV* ranges. The classical approach is well-suited for Rydberg quasimolecules.

Section 1 presented a history of classical studies of diatomic Rydberg quasimolecules. In these studies one of the goals was to find the energy terms of this system – the dependence of the energy of the electron on the internuclear distance. There were three energy terms found, two of them crossing; the crossing had a *V*-shape.

In Section 2, we considered diatomic Rydberg quasimolecules subjected to a static electric field parallel to the internuclear axis. First, it led to the appearance of the fourth energy term, which was absent at the zero field. This term had a *V*-crossing with the lowest energy term. Second – more importantly – the electric field caused additional crossings and these crossings had an *X*-shape. The *X*-crossings occurred at much larger internuclear distances than the *V*-crossings, and one of them was found to significantly enhance charge exchange.

In Section 3, diatomic Rydberg quasimolecules were considered in a plasma of a given screening length, which altered the original potential of either nucleus by an exponential factor (see (3.1)). As in the previously mentioned case, the screening led to the appearance of the fourth energy term having a V-type crossing with the lowest energy term. More importantly, it was found that the screening stabilizes the nuclear motion for $Z = 1$ and destabilizes it for $Z > 1$. We also found that a so-called continuum lowering in plasmas was impeded by the screening, creating the effect similar to that of the magnetic field and opposite to that of the electric field. The continuum lowering plays a key role in calculations of the equation of state, partition function, bound-free opacities, and other collisional atomic transitions in plasmas.

In Section 4, diatomic Rydberg quasimolecules were studied in a laser field. For the situation where the laser field is linearly-polarized along the internuclear axis, we found an analytical solution for the stable helical motion of the electron valid for wide ranges of the laser field strength and frequency. We also found resonances, corresponding to a laser-induced unstable motion of the electron, that result in the destruction of the helical states. For the case of a circularly-polarized field, polarization plane being perpendicular to the internuclear axis, we found an analytical solution for circular Rydberg states valid for wide ranges of the laser field strength and frequency. For this case we demonstrated also that there is a red shift of the primary spectral component. We showed that both under the linearly-polarized laser field and under the circularly-polarized laser field, in the electron radiation spectrum in the addition to the primary spectral component at (or near) the unperturbed revolution frequency of the electron, there appear satellites. Under a laser field of a known strength, in the case of the linear polarization the observation of the satellites would be the confirmation of the helical electronic motion in the Rydberg quasimolecule, while in the case of the circular polarization the observation of the red shift of the primary spectral component would be the confirmation of the specific type of the phase modulation of the electronic motion. Conversely, if the laser field strength is unknown, both the relative intensities of the satellites and the red shift of the primary spectral component could be used for measuring the laser field strength.

In Section 5, a system consisting of a proton, muon and an electron was studied. It was found that a muonic hydrogen atom can attach an electron, with the muon and electron being in circular states. The technique of the separation of rapid and slow subsystems was used, where the muon represented the *rapid* subsystem and the electron the *slow* subsystem. The energy terms of the rapid muon in the field of the two slow (quasi-static) proton and electron were found – a double-degenerate energy term, which corresponds to stable motion. By analysing the slow subsystem, we derived the validity conditions for separation of rapid and slow subsystems. Finally we showed that the spectral lines emitted by the muon experience a red shift compared to the corresponding spectral lines in a

muonic hydrogen atom. Observing this red shift should be one of the ways to detect the formation of such muonic-electronic negative hydrogen ions. Studies of muonic atoms and molecules, where one of the electrons is substituted by the heavier lepton μ^-, have several applications, such as muon-catalyzed fusion, a laser-control of nuclear processes, and a search for strongly interacting massive particles proposed as dark matter candidates and as candidates for the lightest supersymmetric particle. Additionally, analytical relativistic treatment of the muonic motion was conducted, which showed that the relativistic corrections are relatively small.

References

Section 1
Introduction: Two-Coulomb Center Systems Representing Diatomic Rydberg Quasimolecules

[1.1] F. B. Rosmej, and V. S. Lisitsa, *Phys. Lett.*, **A-244**, (1998), 401.

[1.2] R. C. Isler, and R. E. Olson, *Phys. Rev.*, **A-37**, (1988), 3399.

[1.3] S. S. Churilov, L. A. Dorokhin, Yu. V. Sidelnikov, K. N. Koshelev, A. Schulz, and Yu. V. Ralchenko, *Contributions to Plasma Physics*, **40**, (2000), 167.

[1.4] R.C. Elton, *X-Ray Lasers*, Acad. Press, New York, (1990).

[1.5] F. I. Bunkin, V. I. Derzhiev, and S. I. Yakovlenko, *Sov. J. Quant. Electronics*, **11**, (1981), 981.

[1.6] A. V. Vinogradov, and I. I. Sobelman, *Sov. Phys. JETP*, **36**, (1973), 1115.

[1.7] J. Von Neumann, and E. Wigner, *Phys. Z.*, **30**, (1929), 467.

[1.8] S. S. Gershtein, and V. D. Krivchenkov, *Sov. Phys. JETP*, **13**, (1961), 1044.

[1.9] L. I. Ponomarev, and T. P. Puzynina, *Sov. Phys. JETP*, **25**, (1967), 846.

[1.10] J. D. Power, *Phil. Trans. Roy. Soc.*, London, **A-274**, (1973), 663.

[1.11] I. V. Komarov, L. I. Ponomarev, and S. Yu. Slavyanov, Spheroidal and Coulomb Spheroidal Functions (Nauka, Moscow, 1976), In Russian.

[1.12] St. Böddeker, H.-J. Kunze, and E. Oks, *Phys. Rev. Lett.*, **75**, (1995), 4740.

[1.13] E. Oks, and E. Leboucher-Dalimier, *Phys. Rev. E, Rapid Communications*, **62**, (2000), R3067.

[1.14] E. Oks, and E. Leboucher-Dalimier, *J. Phys.*, **B-33**, 3795.

[1.15] E. Leboucher-Dalimier, E. Oks, E. Dufour, P. Sauvan, P. Angelo, R. Schott, and A. Poquerusse, *Phys. Rev. E, Rapid Communications*, **64**, (2001), 065401.

[1.16] E. Leboucher-Dalimier, E. Oks, E. Dufour, P. Angelo, P. Sauvan, R. Schott, and A. Poquerusse, *Eur. Phys. J.*, **D-20**, (2002), 269.

[1.17] E. Dalimier, E. Oks, O. Renner, and R. Schott, *J. Phys.*, **B-40**, (2007), 909.

[1.18] E. Oks, *Phys. Rev. Lett.*, **85**, (2000), 2084.

[1.19] E. Oks, *J. Phys. B: Atom. Mol. Opt. Phys.*, **33**, (2000), 3319.

[1.20] M. R. Flannery, and E. Oks, *Phys. Rev.*, **A-73**, (2006), 013405.

[1.21] E. Oks, *Phys. Rev.*, **E-63**, (2001), 057401.

[1.22] N. Kryukov, and E. Oks, *Intern. Review of Atomic and Molecular Phys.*, **2**, (2011), 57.

[1.23] A. P. Mishra, T. Nandi and B. N. Jagatap, *J. Quant Spectrosc Rad. Transfer*, **120**, (2013), 114.

[1.24] N. Kryukov, and E. Oks, *Can. J. Phys.*, **90**, (2012), 647.

[1.25] M. R. Flannery, and E. Oks, *European Phys. Journal*, **D-47**, (2008), 27.

[1.26] G. Nogues, A. Lupascu, A. Emmert, M. Brune, J.-M. Raimond, and S. Haroche, in Atom Chips, Edits. J. Reichel and V. Vuletic (Wiley-VCH, Weinheim, Germany), (2011), Ch. 10, Sect. 10.3.3.

[1.27] J. N. Tan, S. M. Brewer, and N. D. Guise, *Phys. Scripta*, **T-144**, (2011), 014009.

[1.28] N. Kryukov and E. Oks, *Intern. Review of Atomic and Molecular Phys.*, 3, (2012), 17.

[1.29] J. S. Dehesa, S. Lopez-Rosa, A. Martinez-Finkelshtein, and R. J. Janez, *Intern. J. Quantum Chemistry*, **110**, (2010), 1529.

[1.30] T. Nandi, *J. Phys. B: At. Mol. Opt. Phys.*, **42**, (2009), 125201.

[1.31] U. D. Jentschura, P. J. Mohr, J. N. Tan, and B. J. Wundt, *Phys. Rev. Letters*, **100**, (2008), 160404.

[1.32] A.V. Shytov, M.I. Katsnelson, and L.S. Levitov, Phys. Rev. Letters 99 (2007) 246802.

[1.33] M. Devoret, S. Girvin, and R. Schoelkopf, *Ann. Phys.*, **16**, (2007), 767.

[1.34] E. Oks, *Eur. Phys. J.*, **D-28**, (2004), 171.

[1.35] L. Holmlid, *J. Phys.: Condensed Matter*, **14**, (2002), 13469.

[1.36] S. K. Dutta, D. Feldbaum, A. Walz-Flannigan, J. R. Guest, and G. Raithel, *Phys. Rev. Lett.*, **86**, (2001), 3993.

[1.37] H. Carlsen, and O. Goscinski, *Phys. Rev.*, **A-59**, (1999), 1063.

[1.38] Day M., Ebel M., *Phys. Rev.*, **B-19**, (1979), 3434-40.

[1.39] Pegg D. J., Griffin P. M., Johnson B. M., Jones K. W., Cecchi J. L., and Kruse T. H., *Phys Rev.*, **A-16**, (1977), 2008-10.

Section 2
Enhancement of Charge Exchange and of Ionization by a Static Electric Field

[2.1] E. Lee, D. Farrelly, and T. Uzer, *Optics Express*, **1**, (1997), 221.

[2.2] T.C. Germann, D.R. Herschbach, M. Dunn, and D.K. Watson, *Phys. Rev. Lett.*, **74**, (1995), 658.

[2.3] C.H. Cheng, C.Y. Lee, and T.F. Gallagher, *Phys. Rev. Lett.*, **73**, (1994), 3078.

[2.4] L. Chen, M. Cheret, F. Roussel, and G. Spiess, *J. Phys.*, **B-26**, (1993), L437.

[2.5] R.G. Hulet, E.S. Hilfer, and D. Kleppner, *Phys. Rev. Lett.*, **55**, (1985), 2137.

[2.6] V. M. Vainberg, V. S. Popov, and A. V. Sergeev, *Sov. Phys. JETP*, **71**, (1990), 470.

Section 3
Effect of Plasma Screening on Circular States of Diatomic Rydberg Quasimolecules and their Application to Continuum Lowering in Plasmas

[3.1] E. Oks, Stark Broadening of Hydrogen and Hydrogenlike Spectral Lines in Plasmas: The Physical Insight, *Alpha Science International, Oxford*, (2006), Appendix A.

[3.2] R. P. Drake, *High-Energy-Density-Physics: Fundamentals, Inertial Fusion, and Experimental Astrophysics*, Springer, Berlin, (2006), Sect. 3.2.2.

[3.3] S. Atzeni, and J. Meyer-ter-Vehn, *The Physics of Inertial Fusion: Beam Plasma Interaction, Hydrodynamics, Hot Dense Matter*, Oxford Univ. Press, New York, (2004), Sect. 10.1.4.

[3.4] D. Salzmann, *Atomic Physics in Hot Plasmas*, Oxford University Press, Oxford, (1998), Chapters 2, 3.

[3.5] M. S. Murillo, and J. C. Weisheit, *Phys. Rep.*, **302**, (1998), 1.

[3.6] H. R. Griem, *Principles of Plasma Spectroscopy*, Cambridge University Press, Cambridge, (1997), Sects. 5.5, 7.3.

[3.7] J. Stein, I. B. Goldberg, D. Shalitin, and D. Salzmann, *Phys. Rev.*, **A-39**, (1989) 2078.

[3.8] D. Salzmann, J. Stein, I. B. Goldberg, and R. H. Pratt, *Phys. Rev.*, **A-44**, (1991) 1270.

[3.9] J. Stein, and D. Salzmann, *Phys. Rev.*, **A-45**, (1992), 3943.

[3.10] P. Malnoult, B. D'Etat, and H. Nguen, *Phys. Rev.*, **A-40**, (1989), 1983.

[3.11] Y. Furutani, K. Ohashi, M. Shimizu, and A. Fukuyama, *J. Phys. Soc. Japan*, **62**, (1993), 3413.

[3.12] P. Sauvan, E. Leboucher-Dalimier, P. Angelo, H. Derfoul,T. Ceccotti, A. Poquerusse, A. Calisti, and B. Talin, *J. Quant. Spectr. Rad. Transfer*, 65, (2000), 511.

Section 4
Helical and Circular States of Diatomic Rydberg Quasimolecules in a Laser Field

[4.1] G. R. Fowles, and G. L. Cassiday, *Analytical Mechanics*, Thomson Brooks/Cole, Belmont, CA, (2005), Sect. 3.6.

[4.2] S.T. Thornton and J. B. Marion, *Classical Dynamics of Particles and Systems*, Thomson Brooks/Cole, Belmont, CA, (2004), Sect. 3.6.

[4.3] D. I. Blochinzew, *Phys. Z. Sow., Union* **4**, 501 (1933).

[4.4] E. Oks, Plasma Spectroscopy, *The Influence of Microwave and Laser Fields*, Springer, New York, (1995), Sect. 3.1.

[4.5] N. Kryukov, and E. Oks, *Canad. J. Phys.*, **92**, (2014), 1405.

Section 5
Attachment of an Electron by Muonic Hydrogen Atoms: Circular States

[5.1] L. I. Ponomarev, *Contemp. Phys.*, **31**, (1990), 219.

[5.2] K. Nagamine, *Hyperfine Interactions*, **138**, (2001), 5.

[5.3] K. Nagamine, and L. I. Ponomarev, *Nucl. Phys.*, **A-721**, (2003), C863.

[5.4] C. Chelkowsky, A. D. Bandrauk, and P. B. Corkum, *Laser Physics*, **14**, (2004), 473.

[5.5] J. Guffin, G. Nixon, D. Javorsek II, S. Colafrancesco, and E. Fischbach, *Phys. Rev.*, **D-66**, (2002), 123508.

[5.6] A. R. P. Rau, *J. Astrophys. Astr.*, **17**, (1996) 113.

[5.7] P. Balling, H. H. Andersen, C. A. Brodie, U. V. Pedersen, V. V. Petrunin, M. K. Raarup, P. Steiner, and T. Andersen, *Phys. Rev.*, **A-61**, (2000), 022702.

[5.8] K. Sakimoto, *Phys. Rev.*, **A-78**, (2008), 042509.

[5.9] D. F. Measday, *Phys. Reports*, **354**, (2001), 243.

[5.10] K. Sakimoto, *Phys. Rev.*, **A-81**, (2010), 012511.

[5.11] J. D. Garcia, N. H. Kwong, and J. S. Cohen, *Phys. Rev.*, **A-35**, (1987), 4068.